Relationship of Convection Initiation and Subsequent Storm Strength to Ensemble Simulated Environmental Conditions during IOP3b of VORTEX Southeast 2017

STANLEY B. TRIER,[a] GLEN S. ROMINE,[a] DAVID A. AHIJEVYCH,[a] RYAN A. SOBASH,[a] AND MANDA B. CHASTEEN[b,c,d]

[a] *National Center for Atmospheric Research, Boulder, Colorado*
[b] *Cooperative Institute for Mesoscale Meteorological Studies, Norman, Oklahoma*
[c] *School of Meteorology, University of Oklahoma, Norman, Oklahoma*
[d] *NOAA/OAR/National Severe Storms Laboratory, Norman, Oklahoma*

(Manuscript received 10 May 2021, in final form 6 July 2021)

ABSTRACT: A 50-member convection-allowing ensemble was used to examine environmental factors influencing afternoon convection initiation (CI) and subsequent severe weather on 5 April 2017 during intensive observing period (IOP) 3b of the Verification of the Origins of Rotation in Tornadoes Experiment in the Southeast (VORTEX-SE). This case produced several weak tornadoes (rated EF1 or less), and numerous reports of significant hail (diameter $\geq$ 2 in.; $\geq\sim$5 cm), ahead of an eastward-moving surface cold front over eastern Alabama and southern Tennessee. Both observed and simulated CI was facilitated by mesoscale lower-tropospheric ascent maximized several tens of kilometers ahead of the cold-frontal position, and the simulated mesoscale ascent was linked to surface frontogenesis in the ensemble mean. Simulated maximum 2–5 km AGL updraft helicity (UH_{max}) was used as a proxy for severe-weather-producing mesocyclones, and considerable variability in UH_{max} occurred among the ensemble members. Ensemble members with $UH_{max} > 100\ m^2\ s^{-2}$ had stronger mesoscale ascent than in members with $UH_{max} < 75\ m^2\ s^{-2}$, which facilitated timelier CI by producing greater adiabatic cooling and moisture increases above the PBL. After CI, storms in the larger UH_{max} members moved northeastward toward a mesoscale region with larger convective available potential energy (CAPE) than in smaller UH_{max} members. The CAPE differences among members were influenced by differences in the location of an antecedent mesoscale convective system, which had a thermodynamically stabilizing influence on the environment toward which storms were moving. Despite providing good overall guidance, the model ensemble overpredicted severe weather likelihoods in northeastern Alabama, where comparisons with VORTEX-SE soundings revealed a positive CAPE bias.

KEYWORDS: Fronts; Severe storms; Ensembles; Mesoscale forecasting

1. Introduction

Severe weather outbreaks in the southeastern United States frequently occur during the cool and transition seasons (e.g., Brooks et al. 2003; Smith et al. 2012; Thompson et al. 2012; Childs et al. 2018) within active synoptic patterns containing translating baroclinic systems (e.g., Galway and Pearson 1981; Gaffin and Parker 2006; Sherburn et al. 2016). Although the passage of these midlatitude weather systems are generally well predicted, forecasting the likelihood of severe weather and tornadoes in the Southeast remains a significant challenge for operational meteorologists at all lead times (e.g., Anderson-Frey et al. 2019; Ellis et al. 2019).

Compounding the severe weather forecasting challenge is the disproportionally large number of tornado fatalities occurring in this region owing to the unique overlap of complex meteorological factors and societal vulnerabilities (e.g., Ashley 2007; Strader and Ashley 2018; Anderson-Frey et al. 2019; Agee and Taylor 2019). For instance, tornadoes in the Southeast are produced by a variety of convective modes (e.g., Trapp et al. 2005; Smith et al. 2012; Thompson et al. 2012; Grams et al. 2012; Ashley et al. 2019; McDonald and Weiss 2021), frequently develop at night (e.g., Kis and Straka 2010; Krocak and Brooks 2018), and often occur in only weakly unstable, heterogeneous, or rapidly evolving thermodynamic environments (e.g., Guyer and Dean 2010; Davis and Parker 2014; Sherburn and Parker 2014; King et al. 2017; Coleman et al. 2018). Furthermore, severe events in the Southeast may comprise multiple convective episodes such that antecedent convection influences the mesoscale environment and leads to increased forecast uncertainty (e.g., Chasteen and Koch 2021a,b).

Severe weather outbreaks in the Southeast can contain widespread strong tornadoes that result in numerous injuries and fatalities (e.g., Knupp et al. 2014; Chasteen and Koch 2021a,b), though the majority of southeast severe weather outbreaks contain significantly weaker and more isolated tornadoes. However, Anderson-Frey et al. (2019) concluded that the successful detection and warning of weaker (and less deadly) tornadoes is more difficult. Herein, we use serial radiosonde data and a 50-member convection-allowing ensemble simulation to diagnose mesoscale factors that contribute to severe weather within an eastward-translating baroclinic system on 5 April 2017 during the Verification of the Origins of Rotation in Tornadoes Experiment in the Southeast (VORTEX-SE) Experiment (hereafter VSE).

Coleman and Ancell (2020) used ensemble sensitivity analysis (ESA, e.g., Hakim and Torn 2008) to subset convection-allowing ensembles. Their ensemble subsets reduced error in updraft

Corresponding author: Stanley B. Trier, trier@ucar.edu

Publisher's Note: This article was revised on 12 October 2021 to correct the references for Chasteen and Koch (2021a,b).

DOI: 10.1175/MWR-D-21-0111.1

helicity UH forecasts in an idealized framework, implying potential for successful use of ensemble subsets in severe weather prediction. UH has been used successfully as a severe storm surrogate for prediction with convection-allowing models (e.g., Kain et al. 2008; Sobash et al. 2011, 2016, 2019), and its utility arises from its delineation of updraft rotation in mesocyclones (e.g., Lemon and Doswell 1979), which are often associated with tornadoes or other forms of severe weather (e.g., large hail or strong surface winds). In the current study we form ensemble subsets, based on maximum UH values (section 3b), for diagnostic purposes in a physical process study that evaluates mesoscale environmental factors that influence CI and subsequent severe weather. A similar approach employed by Trier et al. (2019) constructed ensemble subsets based on model-derived radar reflectivity features in simulated storms to determine environmental factors most important to initiation of supercell convection in the lee of the Rocky Mountains in Colorado.

Among the goals of the VSE research program is to reduce damage, injuries, and loss of life from tornadoes through improvements in understanding, forecasting, and warning, in ways that support protective decision making. In the current study we investigate physical processes germane to the understanding and forecasting of CI and the evolution of severe weather environments in the Southeast. In particular, we examine potentially competing roles of mesoscale ascent near a synoptic cold front and environmental modifications influenced by an antecedent mesoscale convective system (MCS) toward which the cold front is advancing.

Diagnostic approaches that link such mesoscale vertical circulations to frontogenesis are well established from theory (e.g., Keyser et al. 1988), and case studies using field observations have documented such circulations and their likely influence on CI (e.g., Ogura and Portis 1982; Trier et al. 1991). However, organized antecedent deep convection can modulate the synoptic environment, resulting in either enhancement (e.g., Chasteen and Koch 2021b) or suppression (e.g., Stensrud and Maddox 1988) of subsequent deep convection.

In section 2 we provide an overview of the environmental conditions diagnosed using a combination of conventional data and VSE field observations, the CI, and severe weather occurrence during the afternoon and early evening portion of IOP3b. The characteristics of our convection-allowing ensemble modeling system and our method for constructing ensemble subsets are discussed in section 3. Simulated convection, and its comparison with observations are presented in section 4. In section 5 we present ensemble mean environmental conditions and diagnose mesoscale processes influencing CI. In section 6 ensemble variability, along with relationships between storm strength and simulated environmental conditions, are examined.

2. Overview of observations over the VSE region during IOP3b

Afternoon CI during IOP3b coincided with the approach of a 500-hPa trough (Fig. 1) and passage of its associated surface cold front across the southeastern United States. The CI of particular interest (CI2) occurred over northern Alabama and

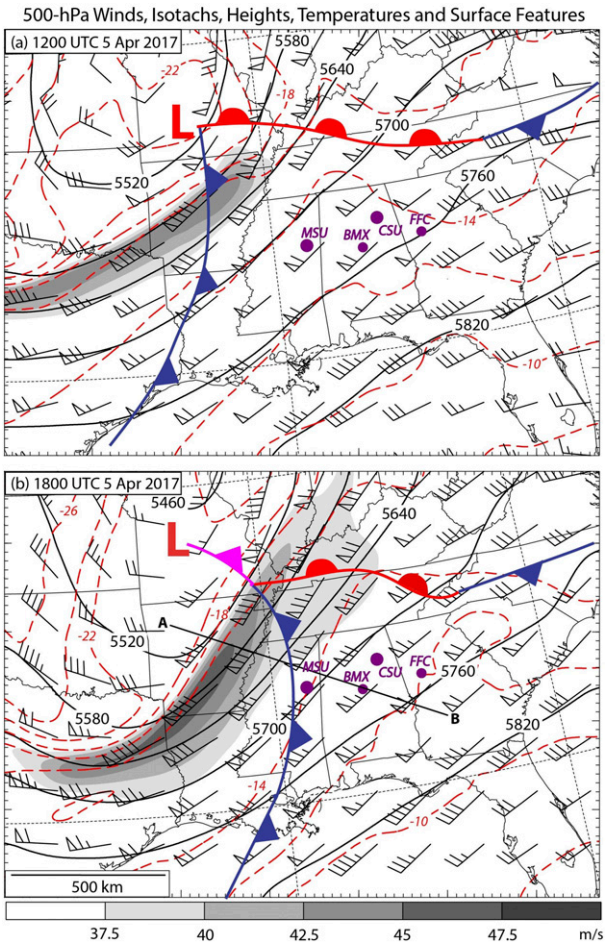

FIG. 1. Ensemble-mean analysis of 500-hPa winds (half barb = 2.5 m s^{-1}, full barb = 5 m s^{-1}, and pennant = 25 m s^{-1}; 1 m s^{-1} = 1.95 kt), geopotential heights (solid contours, 60-m contour interval), and temperature (dashed red contours, 2°C intervals) at (a) 1200 UTC (t = 6 h), and (b) 1800 UTC (t = 12 h) 5 Apr 2017. Colored lines with symbols represent the position of surface cold (blue), warm (red), and occluded (pink) fronts, and the L symbols indicates the positions of surface cyclones. The violet annotations indicate locations of radiosonde data analyzed in Figs. 3 and 6. The transect AB locates the position of the vertical cross sections shown in Fig. 22. The gray shading represents wind speed (m s^{-1}).

southern Tennessee around 2015 UTC (Fig. 2a), and was located between the eastward-moving surface cold front and convection associated with an earlier episode of CI (CI1) that formed behind a large MCS.

Lower-tropospheric convergence and upward motion ($\omega < 0$), where $\omega = Dp/Dt \approx -\rho g w$ (Fig. 3), are diagnosed over a mesoscale triangle near the southern terminus of the CI2 region (Fig. 2a) using VSE radiosonde observations from Mississippi State University (MSU;, Brown 2018) and Colorado State University (CSU; Schumacher and Nielsen 2018), and a supplemental 2034 UTC National Weather Service (NWS) radiosonde from near Birmingham, Alabama (BMX). This application of the kinematic method is identical to that described in recent studies (Trier et al. 2017, 2020) from the Plains Elevated

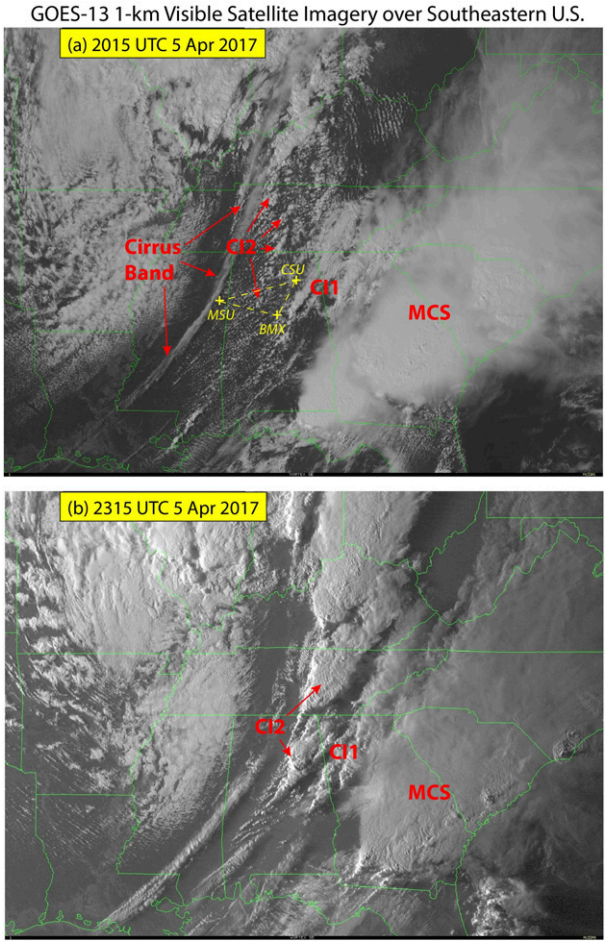

FIG. 2. *GOES-13* 1-km-pixel-resolution visible satellite imagery displayed over the southeastern United States at (a) 2015 and (b) 2315 UTC 5 Apr 2017. The red annotations correspond to cloud features discussed in the text, including the convection initiation (CI) area of primary interest CI2. The dashed triangle formed by the MSU (1957 UTC), CSU (2001 UTC), and BMX (2034 UTC) radiosondes in (a) indicates the region over which mesoscale diagnostics are presented in Fig. 3.

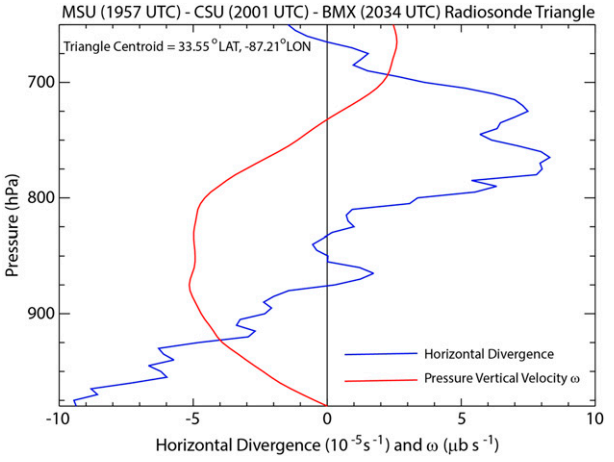

FIG. 3. Mesoscale horizontal divergence and pressure vertical velocity estimates diagnosed from VSE radiosonde observations over the MSU–CSU–BMX radiosonde triangle depicted in Fig. 2a.

Convection at Night Experiment (PECAN; Geerts et al. 2017), except that no upper boundary condition on ω is imposed in the current case because the kinematic calculation is only extended up to 610 hPa, where the MSU sounding terminates. Errors in ω, owing to the vertically integrated effect of systematic radiosonde wind errors, are much less in kinematic vertical motion calculations terminating in the middle troposphere than near the tropopause, where an upper boundary condition of $\omega = 0$ is often applied.

The first CI2 storms developed within a region of mesoscale convergence at the northern edge of an objectively analyzed surface potential temperature maximum located ahead of the surface cold front (Fig. 4a) and near the northwest edge of a surface mixing ratio maximum (Fig. 4b). The greater surface westerly component near the surface temperature maximum than within the moister air over eastern Alabama (Figs. 4a,b) augmented mesoscale convergence ahead of the surface front, consistent with the lower-tropospheric ω minimum diagnosed in Fig. 3.

The CI2 storms produced large downstream anvils evident from visible satellite imagery 3 h later (Fig. 2b), but remained relatively isolated within a broken line of strong storms from central to northeastern Alabama (Fig. 4c). Meanwhile, the convection that arose from the earlier CI episode (CI1, Fig. 2a) persisted near the central Alabama–Georgia border region in cooler (Fig. 4c), but moister (Fig. 4d) surface conditions closer to the rear of the MCS.

Both CI episodes produced severe weather reports over the VSE region (indicated by the dashed rectangles in Fig. 5). The earlier reports in east-central Alabama (Fig. 5a), including a single tornado, were associated with the storms that evolved from CI1 (Fig. 2a), whereas the later reports, mostly occurring between BMX and CSU (Fig. 5b), were from storms that evolved from CI2 (Figs. 2a,b). Most of these later reports were of significant (≥2 in. diameter; ≥~5 cm) hail, which were associated with one or more centers related to reflectivity core 1 in Fig. 4d. The CI2 storms evolved into a continuous evening squall line (Figs. 4e,f) that was not associated with any concentrated regions of severe weather reports (Fig. 5c).

CI1 and CI2 produced a comparable amount of severe weather, but the environment surrounding the CI2 storms was particularly well sampled by VSE and supplemental NWS radiosondes. Thus, we focus the remainder of our analysis on this later CI episode and the evolution of the environment near these afternoon and early evening storms. The 2034 UTC 5 April BMX sounding (Fig. 6a, blue curves) was located near the southern end of CI2 (cf. Fig. 2a), and exhibits favorable CI conditions, with less than 10 J kg^{-1} of CIN and moderate CAPE of 1360 J kg^{-1} for a PBL air parcel averaged through the lowest 500 m. The large 0–500 m AGL averaged mixed layer (ML) to 6-km bulk vertical shear (hereafter, simply bulk vertical shear) of 34 m s^{-1} favored supercell storm organization, which is consistent with the large, relatively isolated cores of

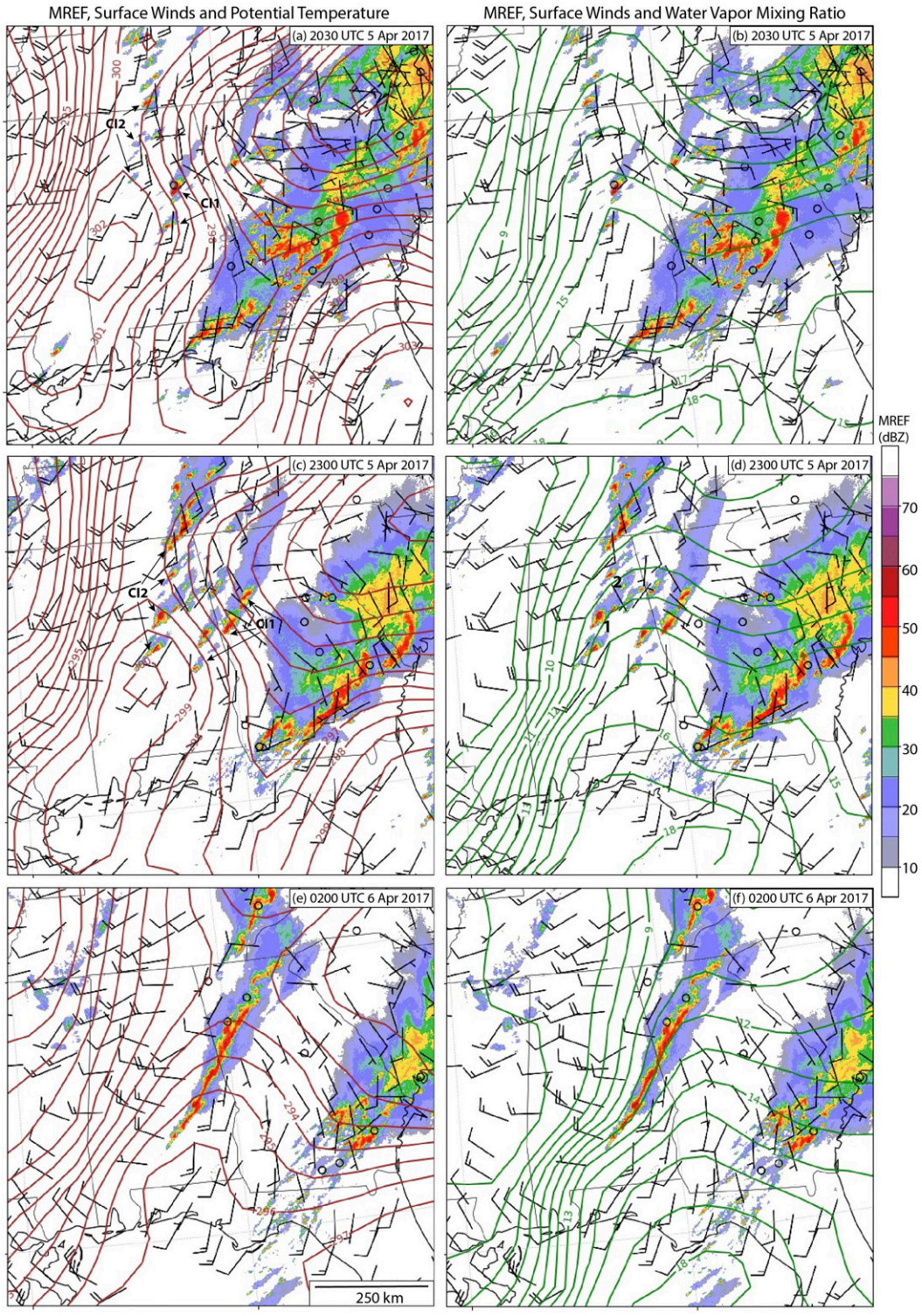

FIG. 4. Surface winds, NEXRAD WSR-88D mosaics of maximum reflectivity in a vertical column (MREF), and objectively analyzed surface (a),(c),(e) potential temperature (brown contours with 1-K intervals), and (b),(d),(f) water vapor mixing ratio (green contours with 1 g kg^{-1} intervals) at (top) 2030 UTC 5 Apr, (middle) 2300 UTC 5 Apr, and (bottom) 0200 UTC 6 Apr 2017. Winds follow the standard meteorological plotting convention of half barb = 5 kt and full barb = 10 kt (1 kt = 0.514 m s^{-1}).

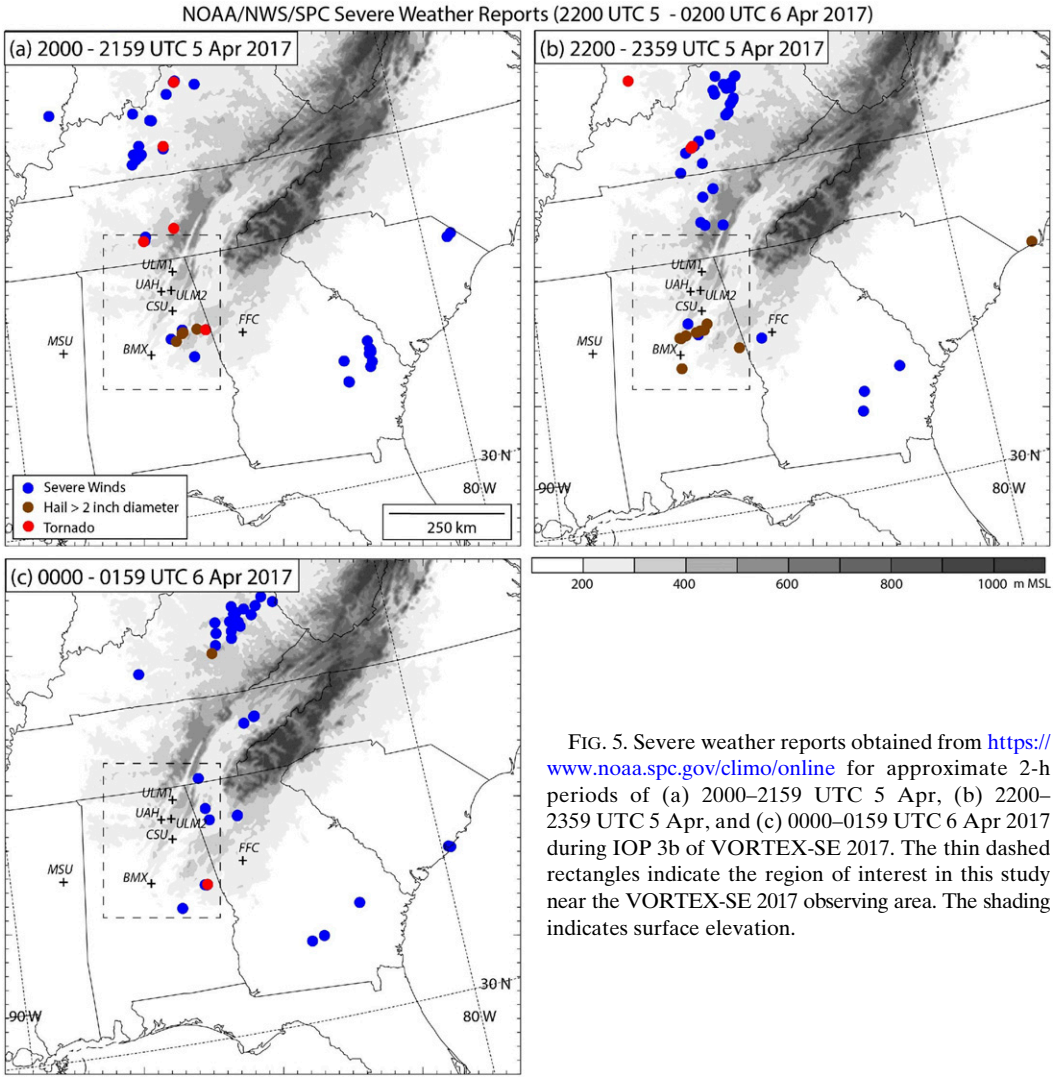

FIG. 5. Severe weather reports obtained from https://www.noaa.spc.gov/climo/online for approximate 2-h periods of (a) 2000–2159 UTC 5 Apr, (b) 2200–2359 UTC 5 Apr, and (c) 0000–0159 UTC 6 Apr 2017 during IOP 3b of VORTEX-SE 2017. The thin dashed rectangles indicate the region of interest in this study near the VORTEX-SE 2017 observing area. The shading indicates surface elevation.

high radar reflectivity over central and eastern Alabama (Figs. 4c,d) and nearby reports of large hail during the next few hours (Fig. 5b).

Environmental thermodynamic conditions were less favorable for severe storms ~2.5 h later in the metropolitan Atlanta area at FFC (Fig. 6a, red curves). In this sounding, the 900–850-hPa layer is supportive of deep convection, but air parcels originating from within this layer must overcome a dry inversion layer above. The less favorable thermodynamic conditions near the surface are related to strong PBL stabilization in the wake of the MCS. The easternmost broken line of storms in western Georgia at 2300 UTC (Figs. 4c,d) reached FFC about 2 h later, but were no longer associated with widespread severe weather (Figs. 5b,c).

Northeast of BMX, afternoon surface warming and PBL growth occurred at the CSU radiosonde site (Fig. 6b) in an environment where moisture increased substantially from west to east across Alabama (Fig. 4d). Consistent with mesoscale ascent (Fig. 3), the inversion located near 800 hPa at 1900 UTC was removed by 2200 UTC (Fig. 6b). Together, these effects resulted in favorable thermodynamic conditions for a 500-m-deep surface-based air parcel in the late afternoon, with MLCAPE of 2270 J kg^{-1} and MLCIN of 25 J kg^{-1}. This later sounding (red curves) had similar CAPE with negligible CIN in the nearly saturated layer from 900 to 850 hPa located directly above the PBL at 2200 UTC (Fig. 6b). Furthermore, the southeasterly flow in the PBL (Fig. 6b, blue and red wind barbs) contributed to even larger values of bulk vertical shear (>40 m s^{-1}) than observed earlier in the CI environment at BMX (Fig. 6a, blue wind barbs).

3. Numerical model and experiment design

a. Convection-allowing WRF ensemble

We now use a 50-member version of the NCAR real-time ensemble modeling system (e.g., Schwartz et al. 2019) to further analyze environmental conditions supporting severe convection. The model contains 39 vertical levels and has an outer domain

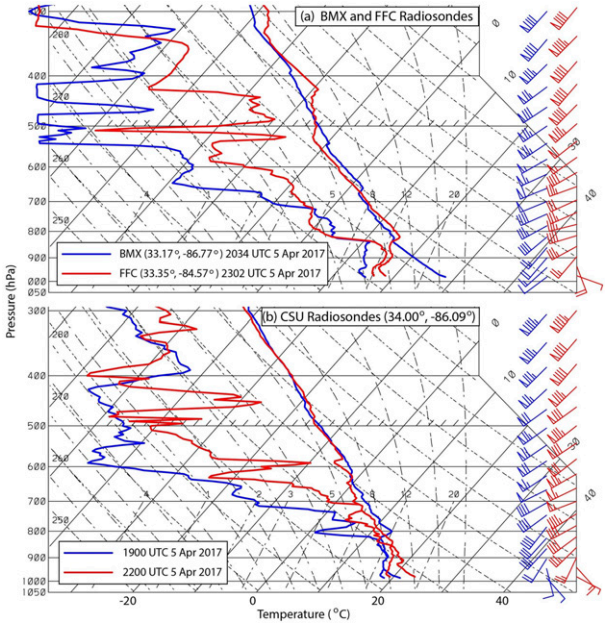

FIG. 6. (a) NWS radiosonde data (UCAR/NCAR–Earth Observing Laboratory 2017) from KBMX (near Birmingham, AL) and KFFC (near Atlanta, GA) from soundings launched at the indicated times. (b) VSE soundings collected by the Colorado State University (CSU; Schumacher and Nielsen 2018) radiosonde team with surface launches at the indicated times. Locations are shown in Fig. 1, and the wind plotting convention is as in Fig. 1.

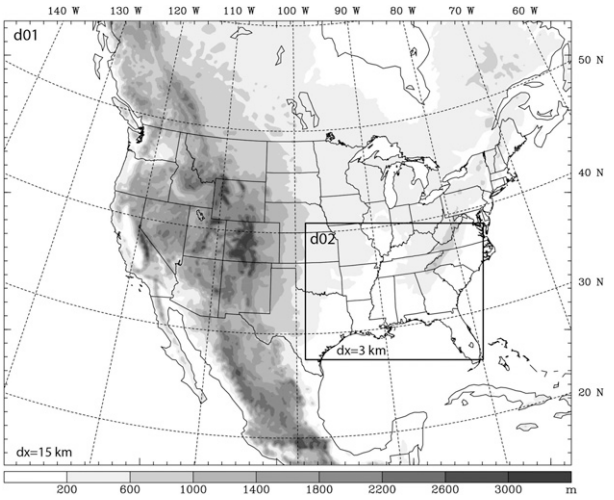

FIG. 7. Model domains for the 50-member ensemble simulations described in this paper. The horizontal grid spacing is indicated within each domain. The shading indicates surface elevations.

d01 (Fig. 7) of 415 × 315 horizontal grid points with spacing of 15 km in which cumulus parameterization (Tiedtke 1989; Zhang et al. 2011) is employed. The inner nest d02 has the same number of vertical levels, and is convection-allowing using 671 × 481 horizontal grid points with spacing of 3 km. The size and location of d02 differs from the CONUS-scale inner nest of the real-time ensemble (Schwartz et al. 2019), and is constructed specifically to simulate convection over the southeastern United States (Fig. 7), including the VSE region. The ensemble uses version 3.6.1 of the Advanced Research core of the Weather Research and Forecasting Model (ARW; Skamarock and Klemp 2008; Powers et al. 2017), is initialized at 0600 UTC 5 April 2017, and is integrated through the duration of IOP3b, which ended at 0100 UTC 6 April 2017.

Analyses having 15-km horizontal grid spacing are generated every 6 h using the Data Assimilation Research Test bed (DART; Anderson et al. 2009). Global Forecast System (GFS) analyses and forecasts are perturbed to provide unique d01 (Fig. 7) boundary conditions for each ensemble member (Torn et al. 2006; Schwartz et al. 2015b; Schwartz et al. 2019). Initial condition perturbations for each member are determined by a continuously cycled ensemble Kalman filter analysis system (Schwartz et al. 2015a; Schwartz et al. 2019) and include potential temperature; geopotential height; dry surface pressure; horizontal wind components; water vapor, rain, cloud water, cloud ice, snow and graupel mixing ratios; and number concentrations for rain and cloud ice. Conventional data are assimilated to create an ensemble analysis every 6 h. Since each ensemble member uses the same model configuration, forecast differences among members arise only from the specified differences in initial and lateral boundary conditions (Romine et al. 2014; Schwartz et al. 2015b; Schwartz et al. 2019).

The set of physical parameterizations were selected based on their successful long-term demonstration in the NCAR ensemble project (e.g., Schwartz et al. 2019). These parameterizations include the Thompson et al. (2008) bulk microphysics scheme, the Rapid Radiative Transfer Model for Global Climate Models (RRTMG; Mlawer et al. 1997; Iacono et al. 2008) shortwave and longwave radiation schemes, the Mellor–Yamada–Janjić PBL scheme (Janjić 2001), and the Noah land surface model (Ek et al. 2003).

b. *Construction of convection-allowing subensembles*

The role of environmental conditions on both CI and subsequent storm evolution is examined using the ensemble mean and two independent subsets of the 50-member ensemble. These subensembles include a group with the strongest storms and another with relatively weak storms that are less likely to produce severe weather, including tornadoes. The environmental conditions for each of these two groups are averaged, and these composite conditions are then compared with observations, the ensemble mean, and with each other.

As previously noted, our 50-member ensemble utilizes 3-km horizontal grid spacing, which is too coarse to simulate fine-scale circulations directly responsible for severe weather. Recent studies (e.g., Sobash et al. 2019; Lawson et al. 2021) have indicated improved realism of rotational features at 1 km horizontal grid spacing. However, 3-km horizontal spacings are capable of simulating midtropospheric mesocyclones in severe-weather-producing supercells. The vertically integrated 2–5 km AGL layer updraft helicity,

$$\mathrm{UH} = \int_{z=2\mathrm{km}}^{z=5\mathrm{km}} (w\zeta)\, dz\,,$$

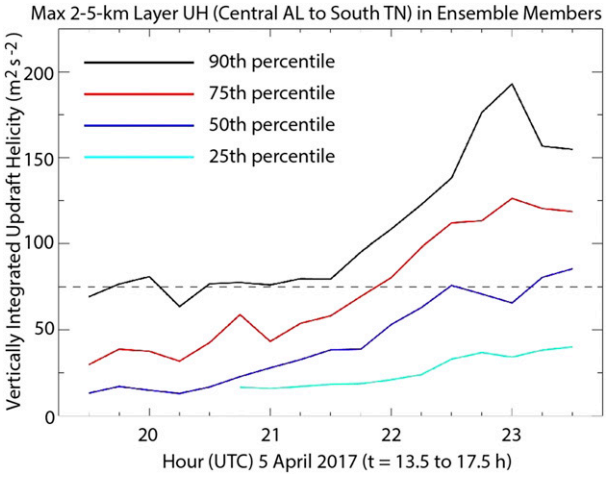

FIG. 8. Percentiles of simulated maximum vertically integrated 2–5 km MSL layer updraft helicity ($m^2 s^{-2}$) occurring within the region indicated by the dashed rectangles in Figs. 5a and 5b.

where w is the vertical velocity and ζ is the vertical component of the relative vorticity, is a useful quantity for identifying midtropospheric mesocyclones in convection-allowing models of similar resolution (e.g., Kain et al. 2008), and its use has been demonstrated to reduce bias in severe weather forecasting. In particular, Sobash et al. (2016) found a UH $> 75\,m^2\,s^{-2}$ threshold to be useful for discriminating between severe and nonsevere weather events in a similarly configured version of the WRF ensemble with identical horizontal resolution.

Maximum values of simulated UH over the dashed rectangular regions in Fig. 5 (hereafter UH_{max}) have been identified for each of the 50 ensemble members from 1930 to 2330 UTC 5 April (forecast lead times of 13.5–17.5 h), and percentile values are plotted in Fig. 8. About half of the ensemble members exceeded the $75\,m^2\,s^{-2}$ severe weather threshold following midafternoon CI. This finding is broadly consistent with the moderate severity and limited duration of the actual severe weather event (Fig. 5), and points toward the potential utility of an ensemble-based physical process study that examines factors influencing severe weather likelihood in uncertain severe storm environments.

To facilitate such an analysis, we constructed two subensembles guided by results from Sobash et al. (2016) and the UH_{max} percentile distributions in Fig. 8. Here, one subensemble (WEAK) contains 8 members where UH_{max} remained significantly less than $75\,m^2\,s^{-2}$ (Fig. 9a), and a second (STRONG) consists of 12 members containing storms with UH_{max} continuously exceeding $100\,m^2\,s^{-2}$ for ≥30 min (Fig. 9b). The STRONG subensemble is a subset of 21 members having $UH_{max} > 100\,m^2\,s^{-2}$, and its 12 members are selected based on storms that attain $UH_{max} > 100\,m^2\,s^{-2}$ being located (at some point in their life cycle) within one of the highlighted areas containing observed storms (Fig. 10a).

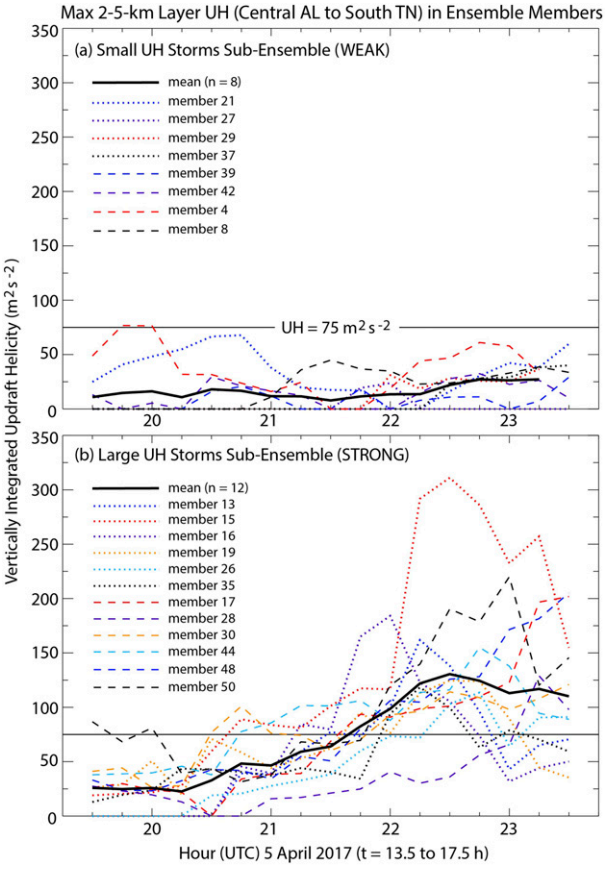

FIG. 9. Time series of maximum vertically integrated 2–5 km MSL layer updraft helicity ($m^2 s^{-2}$) for ensemble members with (a) UH_{max} remaining $<75\,m^2\,s^{-2}$ after 2000 UTC (WEAK subensemble) and (b) UH_{max} exceeding $100\,m^2\,s^{-2}$ (STRONG subensemble) for ≥30 min within the dashed rectangles in Figs. 5a and 5b.

4. Overview of the ensemble simulation and comparison with observations

One factor accounting for variability in storm strength following afternoon CI is related to differences in the position of the antecedent MCS, which, in the observations, is located over eastern and southern Georgia at 2100 UTC (Fig. 10a). The position of the MCS is reasonably well represented in STRONG subensemble member 35 (Fig. 10b); however, southeastward MCS progression is too slow in WEAK subensemble member 27, where active convection on its southwestern flank is erroneously present in east-central and southeastern Alabama (Fig. 10c). This may delay simulated afternoon PBL development and result in the absence of newer simulated convection in member 27 within ellipse 1 over east-central Alabama (Fig. 10c). Though this area of newer convection is simulated in member 35, strong convergence near the rearward outflow of the MCS occurs along the entire NE Alabama–NW Georgia border region, which contributes to this newer convection extending too far north (Fig. 10b).

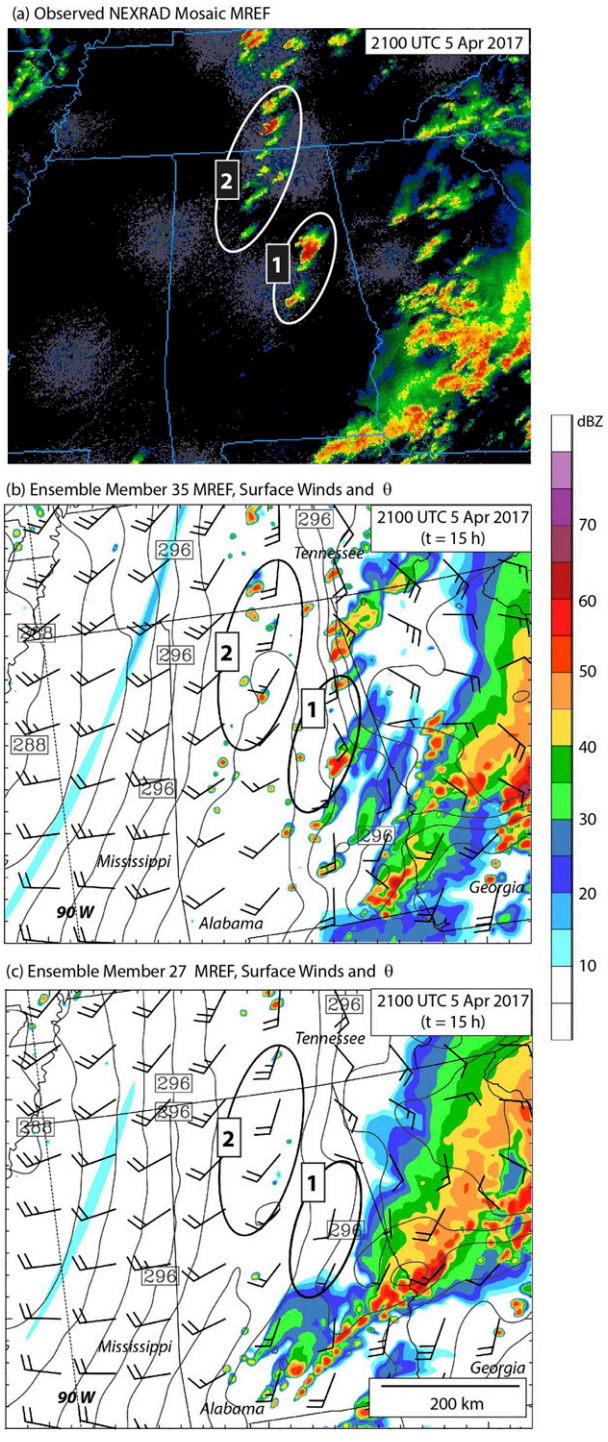

FIG. 10. Maximum radar reflectivity in a vertical column (MREF) at 2100 UTC 5 Apr 2017 from (a) NEXRAD WSR-88D mosaics, and WRF ensemble members (b) 35 and (c) 27. Simulated surface potential temperature is contoured in 2-K increments in (b) and (c) where simulated winds follow the same plotting convention as in Fig. 1. The annotated ellipses specify locations discussed in the text.

There are also differences among ensemble members in the area of newer convection occurring over north-central Alabama and southern Tennessee in ellipse 2 (Figs. 10b,c). This CI corresponds to the initiation region defined earlier as CI2 (Fig. 2a), and is well simulated in member 35 (cf. Figs. 10a,b) but not captured in member 27 (Fig. 10c). In member 35 the CI is located at the downstream edge of an elongated surface potential temperature maximum (Fig. 10b), which has more difficulty developing, and is weaker in member 27 because of position errors in the southwestern part of the ongoing MCS. Ensemble variability in both CI and subsequent storm strength, and their relationships to differences in the surrounding mesoscale environment, are examined further in section 6.

Though simulated reflectivity features at this model resolution are relatively coarse and poorly defined compared to typical radar images of supercells, midlevel mesocyclone circulations are clearly evident in individual members of STRONG (Fig. 11). Within STRONG there are contrasting storm characteristics. This is illustrated by comparing members 26 and 50, which have UH_{max} slightly below the 75th percentile and above the 90th percentile for the full 50-member ensemble (Fig. 8), respectively. Member 26, which has $UH_{max} = 114\,m^2\,s^{-2}$ at 2245 UTC (Fig. 9b), contains a modest $\sim 8\,m\,s^{-1}$ 3.5 km MSL updraft and has a weak surface cold pool of $\Delta\theta \approx -1$ to -2 K (Fig. 11a). In contrast, member 50 has larger UH_{max} of $220\,m^2\,s^{-2}$ at 2230 UTC (Fig. 9b) with a more intense 3.5 km MSL updraft of $\sim 20\,m\,s^{-1}$ and a strong surface cold pool of $\Delta\theta \approx -7$ to -8 K (Fig. 11b). This simulated storm in member 50 was located between BMX and CSU, where most of the observed severe weather between 2200 and 2359 UTC in northern and central Alabama (Fig. 5b) was associated with a simultaneous large isolated storm in the observations (storm 1 in Fig. 4d). In contrast, the maximum UH storm in member 26 is situated ~25 km northwest of the Alabama–Georgia–Tennessee border.

According to climatological studies (e.g., Rasmussen and Blanchard 1998; Thompson et al. 2003, 2007) CAPE values near $2000\,J\,kg^{-1}$ and bulk vertical shear values of 25–30 $m\,s^{-1}$ in the 50-member ensemble mean (Figs. 12a,c) are supportive of severe-weather-producing supercells over central and eastern Alabama from mid-to-late afternoon. This is consistent with numerous ensemble-simulated late afternoon mesocyclone locations with $UH > 100\,m^2\,s^{-2}$ over eastern Alabama (Fig. 12d). On average, these mesocyclone locations are situated northeast of the earlier CI locations within the 50-member ensemble (Fig. 12b).

We define CI in the ensemble simulation and corresponding NEXRAD-WSR-88D mosaics of maximum reflectivity in a vertical column (MREF) as the time when MREF first exceeds 40 dBZ, and this reflectivity is either equaled or exceeded as a trackable reflectivity object for 30 min or more. This storm tracking was performed by visual inspection of the radar mosaics and model output for the individual ensemble members at their 15-min output frequency. Overall, CI locations during 1930–2230 UTC are well represented by the

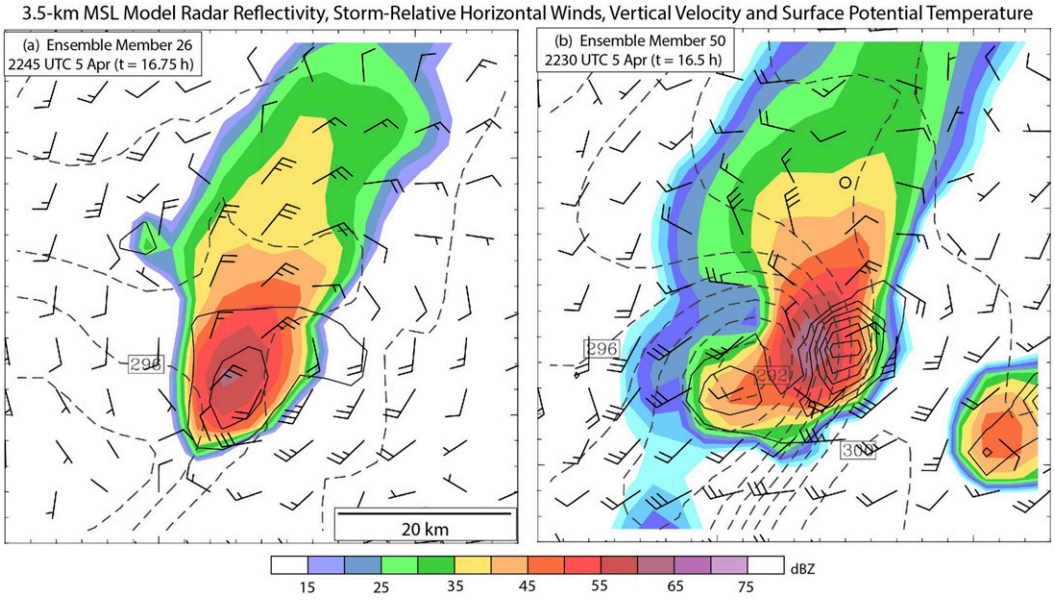

FIG. 11. Storm-relative horizontal winds (half barb = 2.5 m s^{-1}, full barb = 5 m s^{-1}), updraft vertical velocity (solid contours, 3 m s^{-1} contour interval), and model-derived radar reflectivity at 3.5 km MSL for (a) ensemble member 26 at 2245 UTC 5 Apr (forecast hour t = 16.75 h) and (b) ensemble member 50 at 2230 UTC 5 Apr (forecast hour t = 16.5 h). In each panel, the dashed gray contours are of surface potential temperature with 1-K intervals.

ensemble (Fig. 12b), though the ensemble produces some CI too far south and west.

On average, the ensemble mean (MN) overestimates observed (OB) MLCAPE (2100 vs 1440 J kg^{-1}) at the locations of nine VSE convection proximity soundings (Table 1). At BMX (Fig. 12a), which is located toward the southern terminus of the region of observed CI (Fig. 12b), the excess MLCAPE in the ensemble mean (Fig. 13a) results primarily from PBL water vapor mixing ratio that is 2.5 g kg^{-1} larger than observed (Fig. 13c, Table 1), which is influenced by insufficient simulated PBL depth (Fig. 13d), which we estimate from the depth of the surface-based layer of approximately constant θ. The overestimation of MLCAPE and underestimation of daytime PBL depth is commonly reported (e.g., Coniglio et al. 2013; Cohen et al. 2015, 2017) in simulations that use PBL parameterizations with local vertical mixing, such as the MYJ scheme employed in the current ensemble simulation. However, model overestimation of MLCAPE and underestimation of PBL depth does not occur systematically at all sounding locations (Fig. 13d). In contrast, the PBL depth is slightly overestimated by the ensemble mean at most sounding locations north of BMX, and at CSU the ensemble mean MLCAPE is close to that observed (Fig. 13a). At these northeastern Alabama locations the usual fair weather PBL biases expected from past simulations with the MYJ scheme may be dominated by lingering effects associated with the antecedent MCS located farther east (Fig. 10). Though there is an overall positive bias in the simulated MLCAPE, it successfully discriminates between the STRONG and WEAK subensembles at each of the sounding locations (Fig. 14).

In contrast to the MLCAPE, the bulk vertical shear is uniformly underestimated at VSE sounding locations in the ensemble mean (Fig. 13b), and in both the STRONG (ST) and WEAK (WK) subensembles (Table 1). Moreover, unlike for MLCAPE, the bulk vertical shear does not successfully discriminate between the STRONG and WEAK subensembles at each of the sounding locations (Table 1).

Comparison of the ensemble mean, and averages from the WEAK and STRONG subensembles with the observed hodographs (Fig. 15) reveals a layer of primarily westerly shear from the surface to 3 km AGL, and a layer containing weaker southerly shear from 3 to 6 km AGL in each. Despite these common characteristics, the model underestimates the surface to 3 km shear (Fig. 15), which dominates the overall error. However, even with these errors in the bulk vertical shear magnitude, simulated values are still sufficient to support midtropospheric mesocyclones in some ensemble members (Figs. 11, 12c).

Storms with mesocyclones often move in horizontal directions that deviate from the environmental flow (i.e., storm propagation), which is a characteristic that distinguishes supercells from ordinary convection (e.g., Rotunno and Klemp 1982, 1985). This behavior occurs both in observed and simulated storms. For instance, observed storm 1 (Fig. 4d), which evolves from a splitting storm located between BMX and CSU, moves from 252° at 20.5 m s^{-1}. This motion is 7.3 m s^{-1} slower and 17° to the right of the 0–6 km AGL mean flow of 27.8 m s^{-1} from 235° in the 2200 UTC CSU hodograph (Fig. 15b). The average motion of STRONG subensemble member $UH_{max} > 100$ m^2 s^{-2} mesocyclone tracks, which comprise a large majority of mesocyclone

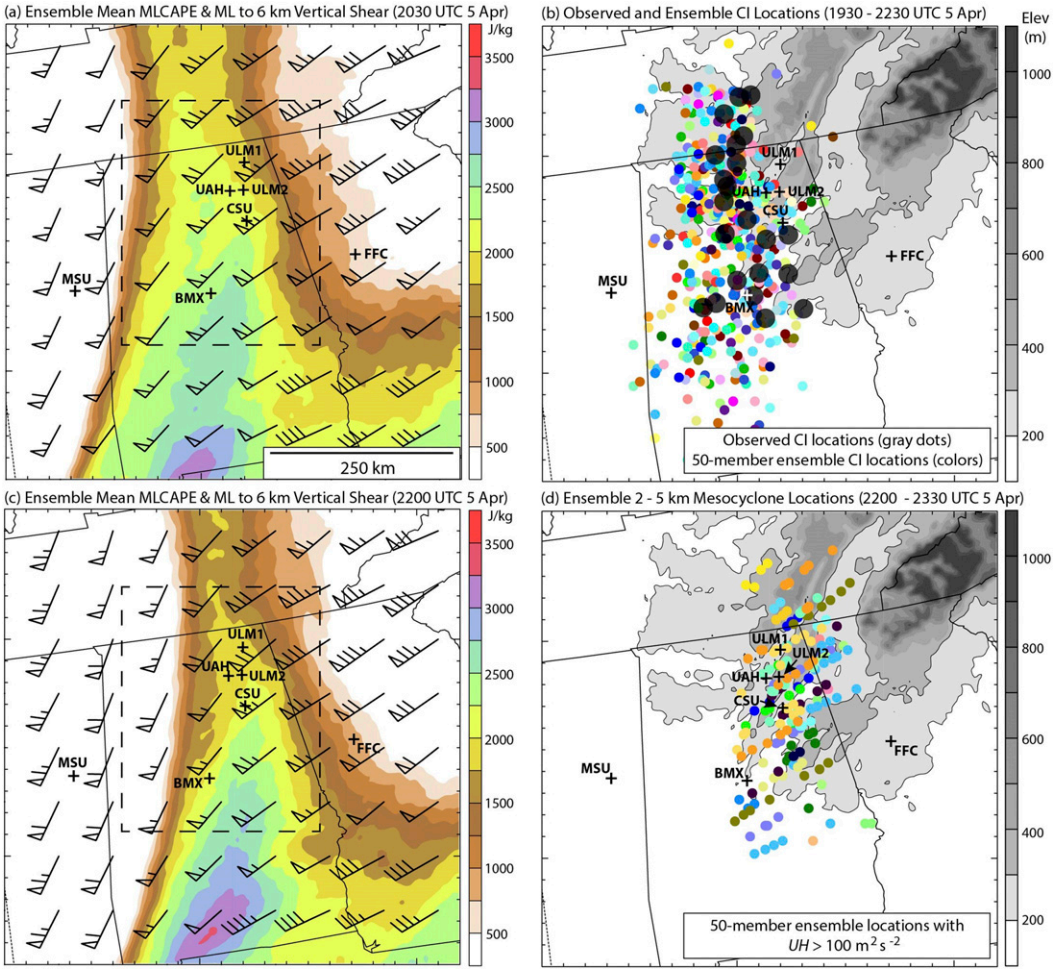

FIG. 12. (left) Ensemble-mean MLCAPE (J kg^{-1}) and wind difference vectors from the mean mixed layer (0–0.5 km AGL) to 6 km AGL for (a) 2030 and (c) 2200 UTC 5 Apr 2017. The wind difference vectors in (a) and (c) follow the plotting convention of Fig. 1 (i.e., half barb = 2.5 m s^{-1}, full barb = 5 m s^{-1}, and pennant = 25 m s^{-1} of bulk vertical shear). (right) Paintball plots of (b) convection initiation (CI) locations from the 50-member WRF ensemble (small colored circles) compared with observations from NEXRAD WSR-88D, (large gray circles) for 1930–2230 UTC 5 Apr 2017 and (d) locations of maximum vertically integrated 2–5-km updraft helicity (small colored circles) exceeding 100 m^2 s^{-2} over the dashed rectangular region in (a) and (c) from 15-min model output for 2200–2330 UTC 5 Apr 2017. Contoured gray shading represents surface elevation. The different colored circles are from different ensemble members.

tracks in Fig. 12d, is from 235° at 19.5 m s^{-1}, and was also 4.5–7 m s^{-1} slower and 12°–20° to the right of the 0–6 km AGL mean flow in average STRONG subensemble hodographs at different locations (Fig. 15).

However, not all observed storms exhibited supercell behaviors. For instance, storm 2 (Fig. 4d) moved only ~3 m s^{-1} slower and 2° to the left of the 0–6 km AGL mean flow at nearby UAH (Fig. 15c), which is characteristic of ordinary thunderstorms and consistent with the lack of any reports of severe weather near UAH (Fig. 5b). Both storms were tracked for 30 min during their mature stages. Storm 1 was tracked from 2310 to 2340 UTC as the right-moving member of the split that occurred immediately after its depiction in Fig. 4d, and storm 2 was tracked from 2240 to 2310 UTC. The differences in behavior between observed storms 1 and 2, despite similar characteristics of the observed CSU (Fig. 15b) and UAH (Fig. 15c) hodographs, suggests that mesoscale CAPE differences (Fig. 14) could be influencing the storms. We examine possible influences of thermodynamic vertical structure on the lack of observed severe storm reports over northeastern Alabama (Fig. 5) in section 6b.

5. Mesoscale processes influencing convection initiation in the ensemble mean

The examination of NWS and VSE soundings in sections 2 and 4 indicated both large spatial variations and rapid

TABLE 1. Observed and simulated convection environment parameters at VSE sounding locations during CI and storm strengthening stages (2000–2200 UTC) on 5 Apr 2017 (OB = VSE sounding, MN = 50-member ensemble mean, ST = 12-member STRONG subensemble mean, and WK = 8-member WEAK subensemble mean).

	MLCAPE (J kg^{-1})				PBL depth (m)				Mean PBL q_v (g kg^{-1})				ML-6 km shear (m s^{-1})			
Site, time (UTC)	OB	MN	ST	WK	OB	MN	ST	WK	OB	MN	ST	WK	OB	MN	ST	WK
BMX, 2034	1360	2460	2610	2290	1400	1000	1100	950	10.5	14.0	14.0	14.0	34	26	27	26
CSU, 2100	2300	2250	2530	1570	500	950	950	850	14.5	13.5	14.0	13.0	44	30	28	31
CSU, 2200	2270	2170	2620	1610	500	950	850	800	14.0	13.0	14.5	13.0	43	29	30	30
UAH, 2008	1320	2000	2210	1510	550	700	900	550	12.5	14.0	13.5	13.0	32	28	29	31
UAH, 2100	1400	2140	2350	1550	600	750	950	650	12.5	13.5	13.5	13.0	35	29	29	30
ULM2, 2039	1210	2100	2310	1400	400	600	700	350	12.0	13.5	13.5	13.0	37	30	30	33
ULM2, 2143	1340	2000	2290	1310	350	700	750	500	12.5	13.0	13.0	12.5	38	29	30	32
ULM1, 2050	870	1880	2050	1270	650	550	650	500	11.5	13.0	12.5	12.5	39	30	30	33
ULM1, 2150	850	1920	2200	1310	700	750	750	650	11.5	12.5	12.5	12.5	42	30	30	32
Avg	1440	2100	2350	1540	650	750	850	650	12.5	13.5	13.5	13.0	38	29	29	31

evolution of the environmental conditions (Fig. 6) supporting convection in the VSE region during IOP3b. In this section these aspects are examined using both horizontal fields and vertical profiles constructed from the 50-member ensemble mean.

Rapid eastward progression of the surface cold front from Mississippi into western Alabama occurs from late morning (Fig. 16a) through midafternoon (Fig. 16c). During this period, strong surface warming ahead of the cold front leads to the elongated potential temperature maximum (Fig. 16c) associated with large MUCAPE increases (Figs. 16a,c) over central and northern Alabama, where afternoon CI occurs (cf. Figs. 12b). As in the observations (Figs. 4a–d) the ensemble mean surface mixing ratio maximum is elongated approximately parallel to surface front and leads the surface potential temperature maximum by approximately 100 km (Fig. 16c).

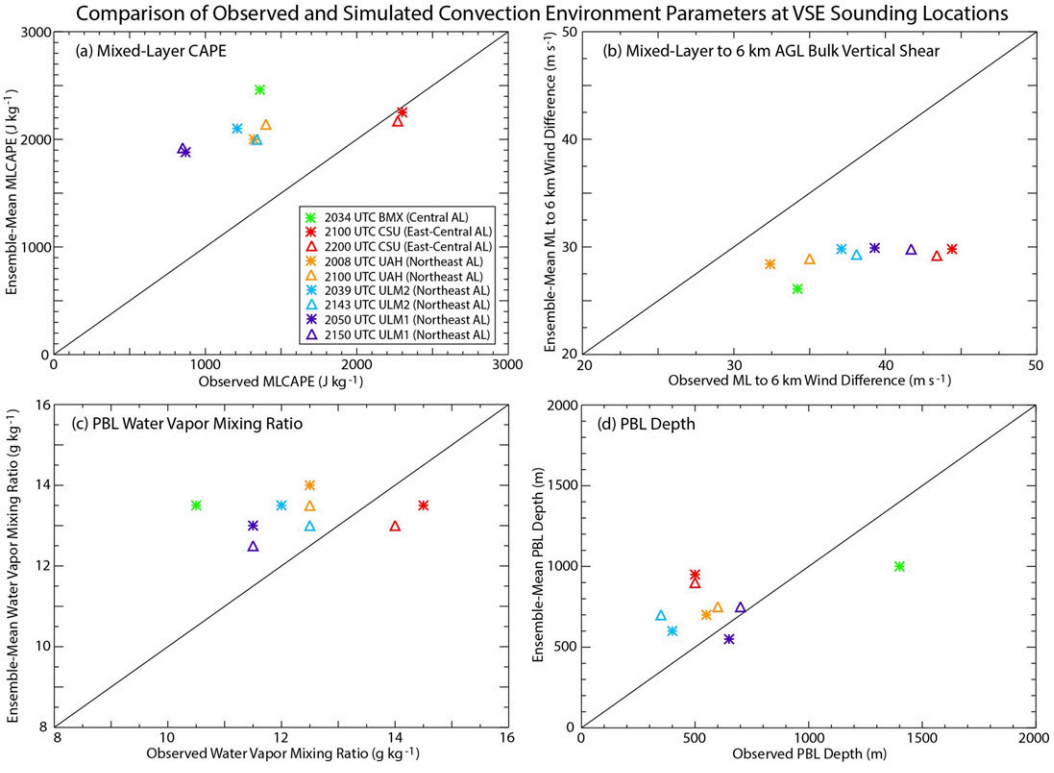

FIG. 13. Comparison of observed and ensemble-mean parameters for the afternoon convection environment at VSE sounding locations shown in Figs. 5 and 12, including (a) mixed-layer CAPE, (b) approximate mean mixed-layer (0–0.5 km AGL) to 6 km AGL vector wind difference (bulk vertical shear), (c) mean PBL mixing ratio, and (d) mean PBL depth.

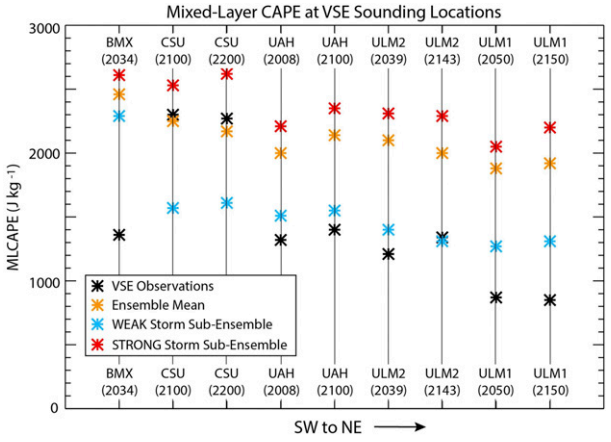

FIG. 14. Observed, 50-member ensemble mean, and means of the 12- and 8-member subensembles STRONG and WEAK mixed-layer CAPE (J kg^{-1}) at the indicated VSE sounding locations (see Figs. 5 and 12).

Meanwhile, the persistence of the MCS and its residual cloud shield (which can be discerned from the widespread late morning midtropospheric ascent in Fig. 16b) limits the eastward extent of significant surface heating and afternoon CAPE increases (Figs. 16a,c). When combined with drying and thermodynamic stabilization behind the eastward-advancing cold front, this aspect contributes to a contraction of the longitudinal extent of moderate-or-greater thermodynamic instability from central to eastern Alabama by midafternoon (Fig. 16c).

Increases in the simulated horizontal gradients of potential temperature and water vapor mixing ratio occur from late morning (Fig. 16a) to midafternoon (Fig. 16c) in the vicinity of the surface cold front. The change in horizontal temperature gradient magnitude following the flow is calculated from the forcing on the right side of the two-dimensional frontogenesis function:

$$F = \frac{D}{Dt}|\nabla_H T| = \frac{|\nabla_H T|}{2}[\mathrm{DEF}\cos(2\beta) - \mathrm{DIV}],$$

where

$$\mathrm{DEF} = \left[\left(\frac{\partial u}{\partial x} - \frac{\partial v}{\partial y}\right)^2 + \left(\frac{\partial v}{\partial x} + \frac{\partial u}{\partial y}\right)^2\right]^{0.5}$$

and

$$\mathrm{DIV} = \frac{\partial u}{\partial x} + \frac{\partial v}{\partial y}$$

are the total horizontal deformation and divergence, respectively, and β is the angle between the isotherms and the axis of dilatation. An elongated region of mean surface frontogenesis ($F > 0$) extends from western Alabama into southern Tennessee at 2030 UTC (Fig. 16d).

In the 2 h prior to afternoon CI surface warming occurs across much of Alabama (Fig. 17a). Northeastern Alabama, which was affected earlier by the MCS, experiences the maximum surface potential temperature increases. In this location, the surface heating that occurs over much of the state is augmented by warm advection within southwesterly surface flow in advance of the surface cold front (cf. Fig. 16c). Cloudiness with the ongoing MCS precludes surface warming over Georgia and southeastern Alabama (Fig. 17a).

The surface warming (Fig. 17a) is surmounted by midtropospheric cooling (Fig. 17b) in the preceding 2 h over central and western Alabama. The cooling aloft (Fig. 17b) has an elongated maximum that nearly coincides with a region of mesoscale ascent in Fig. 16d. The 750-hPa flow is nearly parallel to the isotherms (Fig. 17b), indicating that horizontal temperature advections are weak, and that the cooling above the PBL is likely dominated by adiabatic temperature changes associated with the mesoscale ascent. At the gold circles (Figs. 17a,b), which indicate the approximate centroid of the CI occurrence (cf. Fig. 12b), the surface warming and 750-hPa cooling, are ≈ 2 and ≈ -1 K, respectively. These simultaneous changes destabilize the lapse rate resulting in a 2-h increases of $-\partial T/\partial z \approx 1\ \mathrm{K\ km^{-1}}$.

A vertical cross section (Fig. 18), averaged for 100 km on each side of transect A′B′ in Fig. 16, illustrates the evolution of the mean mesoscale vertical motion prior to afternoon CI in the direction normal to the surface cold front. The ω minimum, indicating lower-tropospheric mesoscale ascent that becomes maximized ~50 km ahead of the surface cold front (Fig. 18b), is associated with deepening positive local moisture tendencies that extend above the PBL (Figs. 18a,b), which act together with the destabilizing lapse rate (Fig. 17) to promote afternoon CI. During the 2-h period immediately prior to CI, the lower-tropospheric ω minimum intensifies above the region of surface frontogenesis (Figs. 18c,d). The depth, location, and intensity of this mesoscale ω minimum near the leading edge of the surface front is broadly consistent with that diagnosed from radiosonde observations in section 2 (Figs. 2a, 3).

A mesoscale midtropospheric vertical motion couplet is located between the leading edge of the surface front (x = 475 km) and a midtropospheric front (x = 175 km), and has a ~90° phase shift between local vertical motion and potential temperature extrema (Fig. 18b), which is characteristic of a gravity wave. This feature does not appear to influence the lower-tropospheric ascent and CI that occurs closer to the position of the surface front (section 6), and is thus not examined further in this study.

Linkages between simulated surface frontogenesis and lower-tropospheric mesoscale ascent are investigated using the Q-vector form of the quasigeostrophic omega equation:

$$\sigma\nabla_p^2\omega + f_0^2\frac{\partial^2\omega}{\partial p^2} = -2\nabla\cdot\mathbf{Q},$$

where σ and f_0 are the domain-averaged static stability and Coriolis parameters, respectively, and the right-hand side of the equation represents the frontogenetical forcing associated with the geostrophic flow (see, e.g., Holton 1992). Though it is somewhat shallower, and centered about 50 hPa lower,

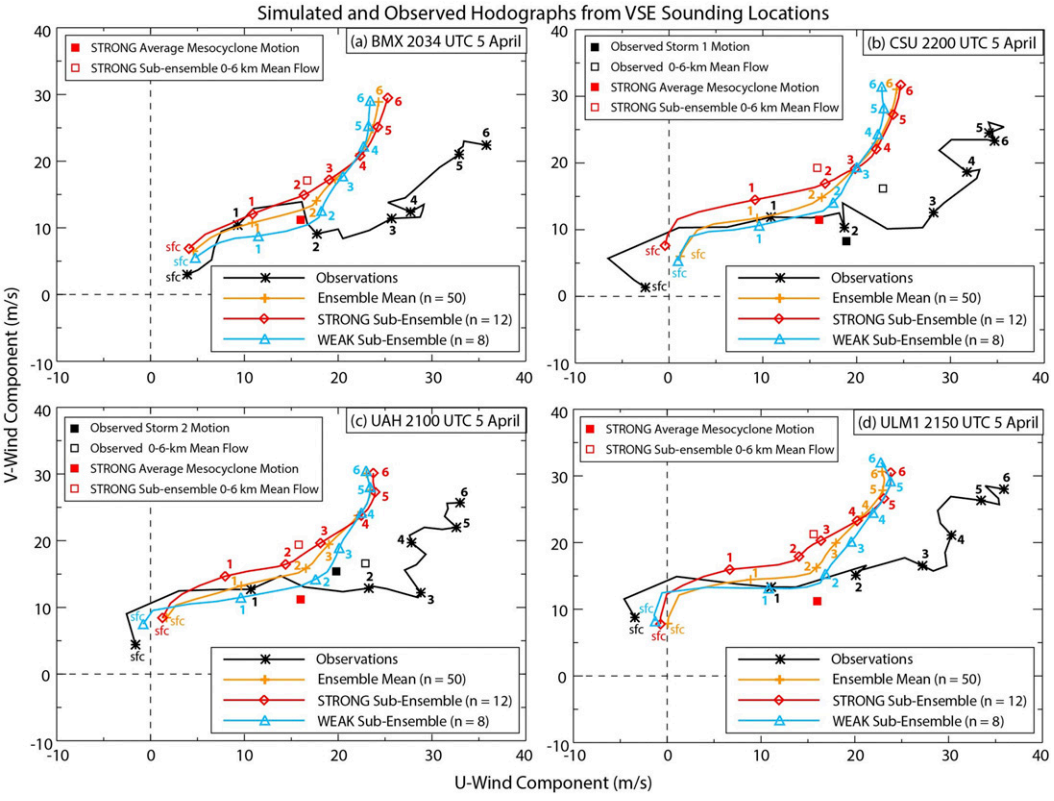

FIG. 15. Observed and ensemble-averaged simulated horizontal wind hodographs at the indicated times from the (a) National Weather Service (NWS) sounding location (BMX) near Birmingham, AL (UCAR/NCAR–Earth Observing Laboratory 2017), (b) Colorado State University (CSU) VSE sounding location (Schumacher and Nielsen 2018), (c) University of Alabama–Huntsville (UAH) VSE sounding location (Pangle and Wade 2020), and (d) University of Louisiana–Monroe VSE sounding location number 1 (ULM1) (Murphy 2018) with annotated heights in (km AGL). The geographic locations of these hodographs are displayed in Figs. 5a–c and Fig. 12. The black square symbols indicate horizontal motions (filled) of annotated storms from Fig. 4d and the 0–6 km AGL mean flow at the hodograph locations (unfilled). The red square symbols indicate the average horizontal motions (filled) of simulated mesocyclones with $UH_{max} > 100\,m^2\,s^{-2}$ and the average 0–6 km AGL mean flow (unfilled) at the corresponding observed hodograph locations in the STORM subensemble.

the quasigeostrophic ω minimum (Figs. 18e,f) reasonably well approximates the total mesoscale ascent (negative ω) in the frontogenesis region along and ahead of the leading edge of the surface cold front (Figs. 18c,d). This relatively good agreement contrasts with the wavelike mid- to upper-tropospheric vertical motion couplet from $x = 250$ to 400 km (Figs. 18c,d), which is poorly represented by the quasigeostrophic solution (Figs. 18e,f).

The intensification and migration of maximum near-surface frontogenesis and mesoscale ascent to a location several tens of km ahead of the front (Fig. 18d) prior to simulated afternoon CI coincided with a greater increase of the near-surface westerly component (Fig. 19b) at the prefrontal location PF than at WT near the eastern edge of the warm tongue (cf. Fig. 17a). Similar shifts in the location of maximum surface frontogenesis have been noted in conjunction with prefrontal troughs and wind shifts (e.g., Schultz 2005), and an afternoon wind shift ahead of the surface front was also apparent in the observations (Figs. 4a,c). In the current case, the simulated increase in westerly component at CF (Fig. 19b, blue curves) is consistent with the downward transport of stronger westerly momentum as the PBL preferentially deepens near and slightly ahead of the front (Fig. 19a, blue curves). Farther east at WT, which is located closer to the MCS wake, the near-surface westerly component does not increase during the same 2-h period (Fig. 19b, red curves), which is consistent with horizontal convergence and upward motion becoming maximized ahead of the surface front between CF and WT (Figs. 18d,f) near the time of simulated CI.

6. Relationship of simulated CI and storm strength to environmental conditions

a. Comparison of the STRONG and WEAK subensembles

A comparison of averages for the STRONG (Fig. 20a) and WEAK (Fig. 20b) subensembles reveal a more intense

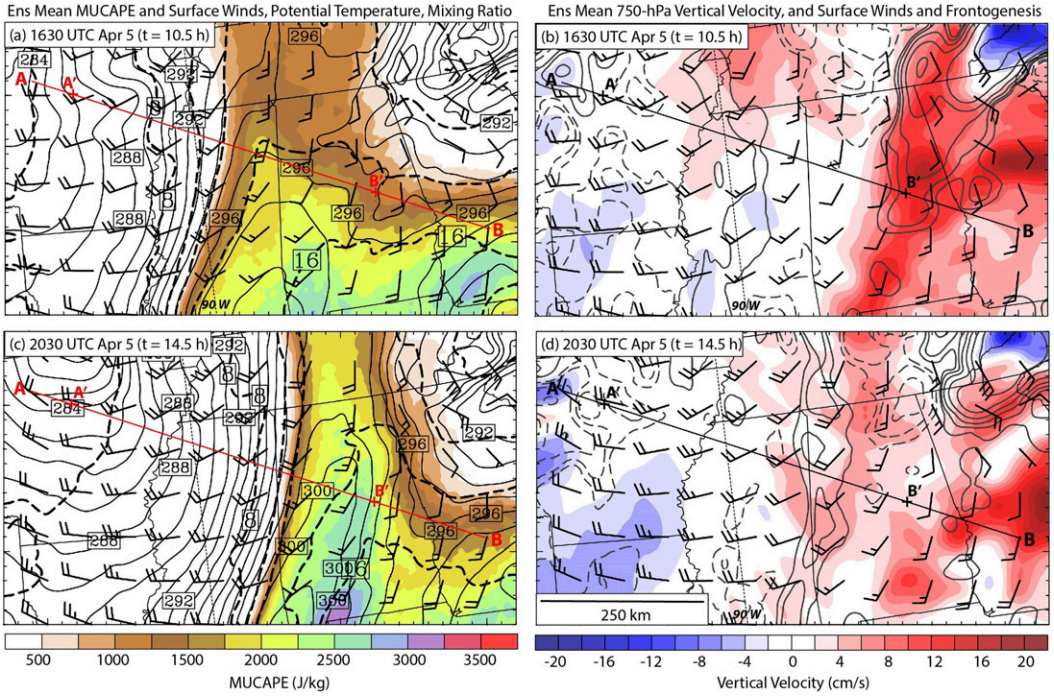

FIG. 16. Ensemble-mean surface winds and (a),(c) surface potential temperature (solid contours, 1-K intervals), water vapor mixing ratio (dashed contours, 2 g kg^{-1} intervals), and convective available potential energy for the highest equivalent potential temperature air parcel of 50-hPa depth (MUCAPE, color shading); and (b),(d) surface frontogenetical function [gray contours, negative contours dashed with values of −32, −16, −8, −4, −2, −1, 1, 2, 4, 8, 16, and 32 K (100 km)$^{-1}$ h^{-1}] and 750-hPa vertical velocity (color shading) at (top) 1630 UTC (forecast hour t = 10.5 h) and (bottom) 2030 UTC (forecast hour t = 14.5 h) 5 Apr 2017. The transect AB indicates the position of the 200-km averaged vertical cross sections presented in Fig. 22, with A′B′ indicating the position of the vertical cross sections in Fig. 18.

surface frontal moisture gradient in STRONG. CI in STRONG occurs in a mesoscale convergence zone located ~50 km ahead of the 2030 UTC mean surface frontal moisture gradient (Fig. 20a). The location of the average CI position in STRONG corresponds well with the western edge of the observed CI (cf. Fig. 20a with the large gray dots in Fig. 12b).

There is 1–2 g kg^{-1} greater surface moisture in STRONG than in WEAK along and slightly ahead of the STRONG surface frontal position (Fig. 21a). The surface moisture excess in STRONG results in larger MUCAPE, and CI occurs in a zone of greater convergence and upward motion at the eastern edge of the larger MUCAPE in STRONG (Fig. 21c), where the surface westerly component becomes weaker (cf. Fig. 20a).

In addition to differences in surface moisture along and ahead of the surface front, the vertical cross section averaged for 100 km on each side of AB (see Fig. 16 for location) reveals excesses and deficits from the ensemble mean mixing ratio directly above the PBL in STRONG (Fig. 22a) and WEAK (Fig. 22b), respectively. These differences in elevated moisture near the surface front are associated with corresponding differences in the strength of the mesoscale ascent between the two subensembles (Figs. 22a,b).

Along with the differences in the lower-tropospheric mesoscale ascent, substantive differences between the two subensembles also occur in the right (southeast) portion of the cross section where deep, widespread, and more intense average vertical motions are a reflection of the ongoing MCS. In WEAK (Fig. 22b), well-organized mid- and upper-tropospheric subsidence along the rear periphery of the MCS extends northwestward to the leading edge of the surface front. This subsidence may act together with the lower-tropospheric moisture deficits (from x = 550–700 km) to both delay CI and hinder subsequent storm strengthening in WEAK (Fig. 22b).

The UH_{max} locations in the STRONG subensemble approximately 2 h later (cyan dots in Fig. 21) confirm, in addition to more favorable conditions in which CI occurs, that maturing convection moves toward eastern Alabama, where MUCAPE values are 500–1000 J kg^{-1} greater than in WEAK (Fig. 21c). These more favorable thermodynamic conditions coincide with both warmer (Fig. 21b) and moister (Fig. 21a) near-surface conditions in STRONG over eastern Alabama, which are influenced by differences in the evolution of the antecedent MCS.

Unlike for MUCAPE, the storms in STRONG move toward a region of slightly weaker bulk vertical shear than

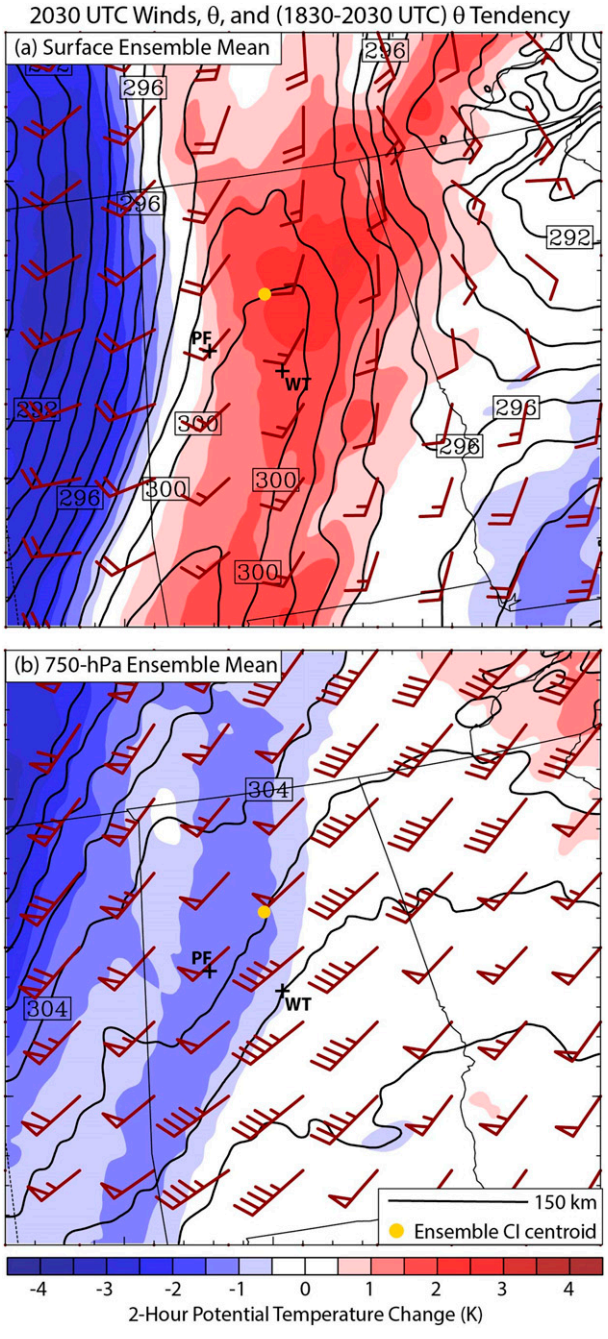

FIG. 17. Ensemble-mean potential temperature (1-K contour interval) and horizontal winds at 2030 UTC 5 Apr 2017 ($t = 14.5$ h), and 2-h potential temperature change ending at 2030 UTC (color shading) at (a) the surface and (b) 750 hPa. The gold circles indicate the approximate central location of afternoon convection initiation in the model and observations. PF and WT indicate horizontal locations of the vertical profile plots in Fig. 19. The winds follow the same plotting convention described in Fig. 1.

in WEAK (Fig. 21d). This results primarily from southerly surface flow in WEAK (Fig. 21b) compared with southwesterly flow in the corresponding region of STRONG, which was more unstable (Fig. 21a). However, as previously noted (Table 1), bulk vertical shear magnitudes in the STRONG subensemble were still sufficient for supercells in northeastern Alabama, as evidenced by simulated mesocyclones with $UH_{max} > 100\,m^2\,s^{-2}$ (Fig. 21).

b. *Forecast considerations*

A tornado watch (WT127) from 1900 UTC 5 April to 0200 UTC 6 April 2017 was issued by NOAA's Storm Prediction Center (SPC) for nearly all of central and northern Alabama. This tornado watch continued northward through middle Tennessee and Kentucky in conjunction with destabilizing thermodynamic conditions ahead of the surface front. In retrospect, the large meridional extent of $UH_{max} > 100\,m^2\,s^{-2}$ storms from eastern Alabama into south-central Tennessee at 2230 UTC 5 April (Fig. 12d) is indicative of widespread severe weather potential from mesocyclones within the model.

However, the actual severe weather reports over the VSE region (Fig. 5) were limited to east-central Alabama, with a separate cluster located over southern Tennessee. Though thunderstorms did occur in northeastern Alabama (Fig. 4d) north of the CSU sounding location, this region was characterized by a lack of severe weather reports during the tornado watch period (Fig. 5). One of the shortcomings of this ensemble simulation is its inability to discriminate environmental conditions less conducive to severe weather in northeastern Alabama from those in nearby regions that experienced severe weather.

The earlier examination of environmental severe weather parameters (Table 1) indicated sufficient bulk vertical shear to support mesocyclones at VSE sounding locations over northeastern Alabama in both observed soundings and collocated model vertical profiles. However, there was a positive bias in simulated MLCAPE at all VSE sounding locations north of CSU (Fig. 13a). Though the observed MLCAPE values of 850–1400 $J\,kg^{-1}$ in northeastern Alabama (Table 1, Fig. 13a) are supportive of severe weather, actual parcel buoyancies may be susceptible to entrainment of dry air above the lower troposphere (Fig. 23b).

We produced a rough estimate of possible entrainment effects on vertically integrated parcel buoyancies in the VSE soundings (Fig. 23, dashed parcel ascent curves) following Davis and Ahijevych (2013) and Trier et al. (2015), which prescribe a constant entrainment rate of 10% per kilometer. This approach separately mixes parcel temperature and vapor mixing ratio with values from environmental air at successive model vertical levels, and is motivated by Romps (2010) and Yeo and Romps (2013), who found similar entrainment rates in large-eddy simulations of deep convection. However, our estimates do not directly account for possible effects of environmental vertical shear, which Mulholland et al. (2021) showed can influence entrainment in squall-line environments.

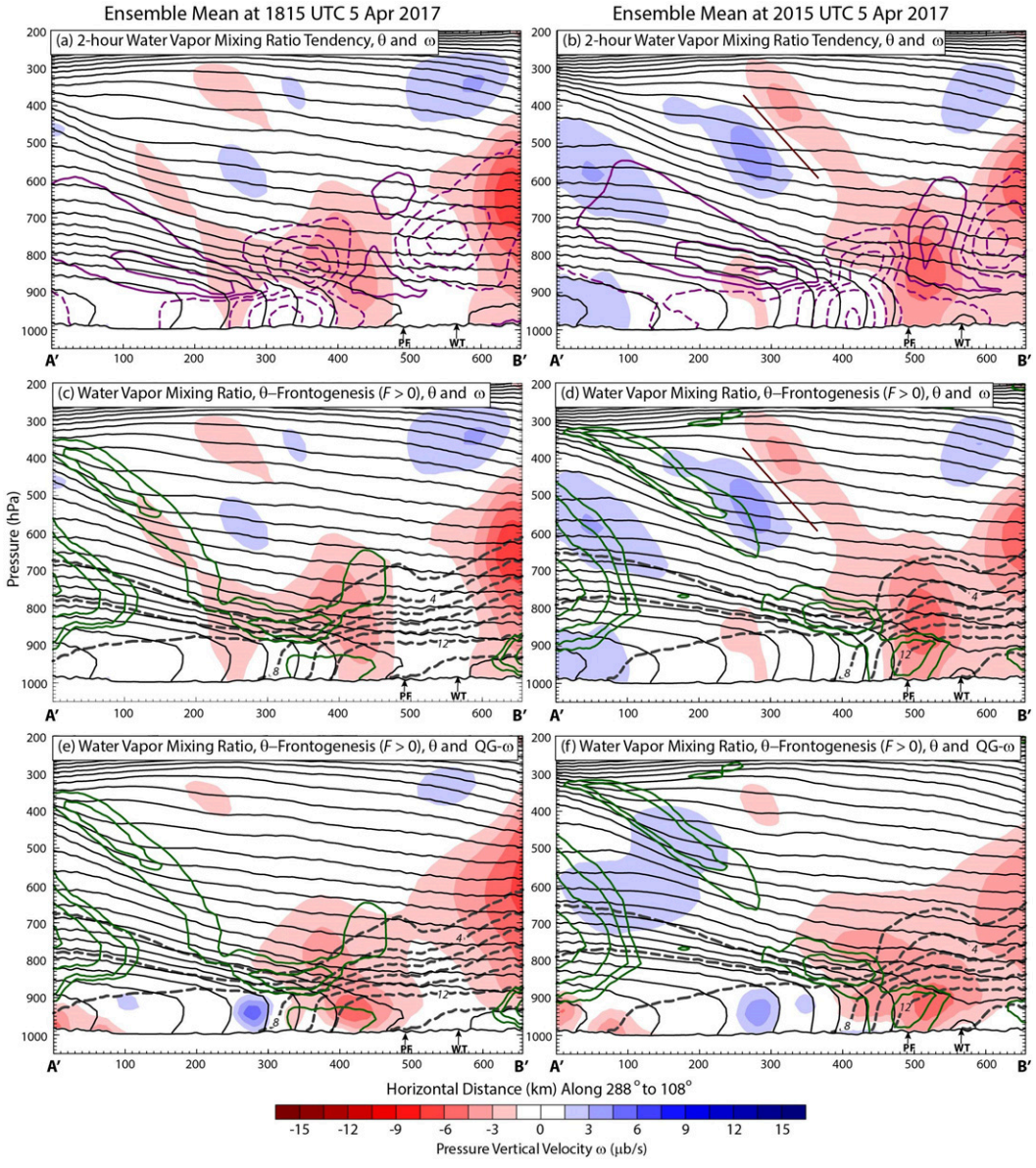

FIG. 18. Ensemble-mean vertical cross sections along transect A′B′ (Fig. 16) averaged for 100 km on each side of A′B′. Potential temperature (thin black contours, 2-K contour interval) and (a),(b) pressure vertical velocity (color shaded), and 2-h water vapor mixing ratio tendency [purple contours, −3.5, −2.5, −1.5, −0.5, 0.5, 1.5, and 2.5 g kg^{-1} values (negative dashed)]; (c)–(f) frontogenesis function [green contours; 1, 2, 4, and 8 K (100 km)$^{-1}$ h^{-1} values] and water vapor mixing ratio (dashed gray contours with 2 g kg^{-1} intervals starting at 2 g kg^{-1}); and (c),(d) pressure vertical velocity (color shaded); and (e),(f) quasigeostrophic pressure vertical velocity (color shaded) at (left) 1815 and (right) 2015 UTC 5 Apr 2017. The bold black line in (b) and (d) indicates the approximate phase line of the ensemble-averaged mesoscale gravity wave discussed in the text. The annotations PF and WT refer to the horizontal locations of the vertical profile plots (Fig. 19) whose horizontal locations are shown in Fig. 17.

For the 2200 UTC CSU sounding, our prescribed entrainment reduces the MLCAPE by about 50% (Fig. 23a). The substantial MLCAPE of ~1100 J kg^{-1} that remains after this large entrainment, together with large bulk shear (Table 1), is consistent with severe weather reports near this location (Figs. 5b,c). However, the MLCAPE reductions from 850 to 280 J kg^{-1} at 2150 UTC for ULM1 (Fig. 23b) in northeastern Alabama may be more significant since they comprise a greater percentage of the original pseudoadiabatic MLCAPE and result in much lower entrainment-modified MLCAPE values than at CSU.

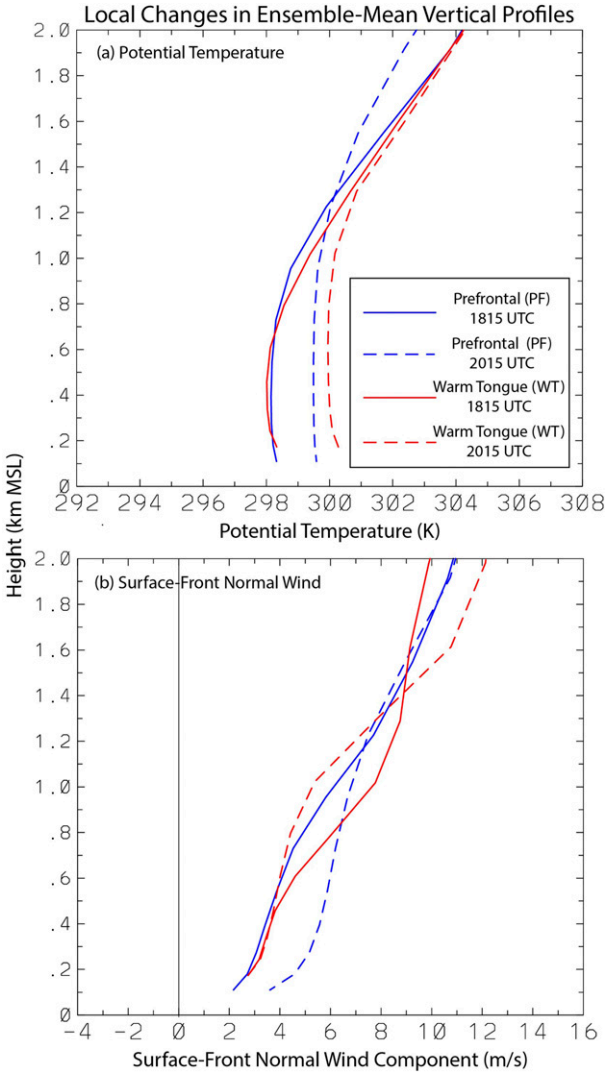

FIG. 19. Ensemble-mean vertical profiles of (a) potential temperature and (b) the component of horizontal flow (along 288°–108°) relative to the motion of the surface cold front at the horizontal locations indicated in Fig. 17 by PF (blue curves) and WT (red curves).

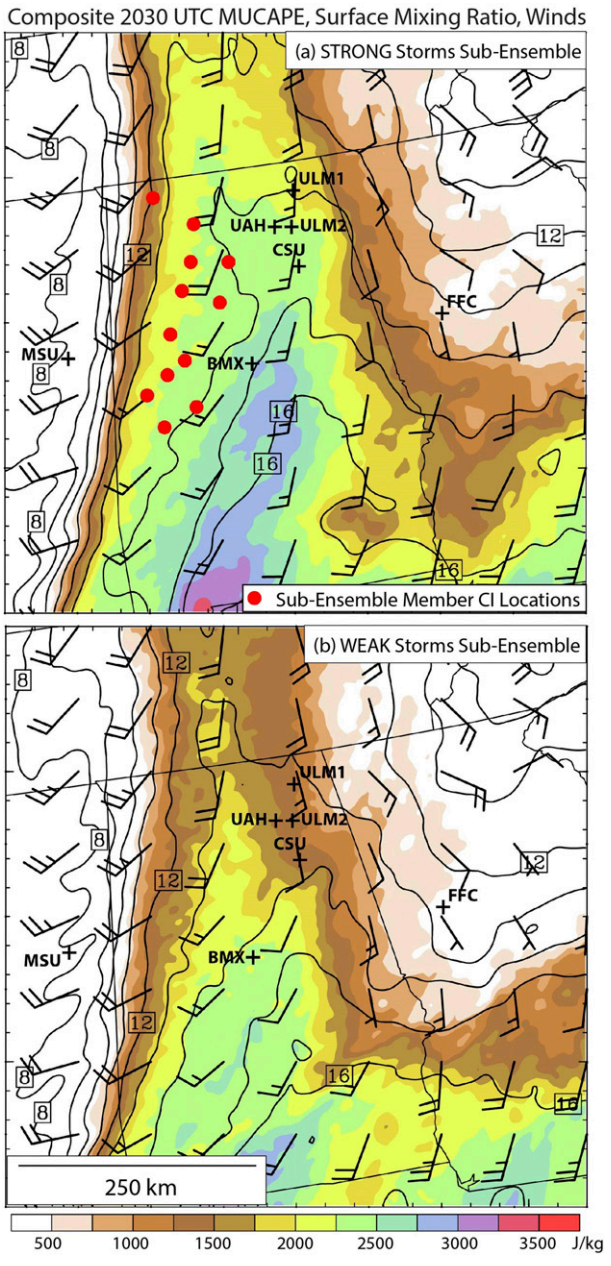

FIG. 20. Average surface horizontal winds, mixing ratio (1 g kg^{-1} contour intervals), and MUCAPE (J kg^{-1}, calculated as in Figs. 12a and 12c) for the (a) STRONG ($n = 12$) and (b) WEAK ($n = 8$) storm subensembles. The red bullets in (a) indicate CI locations for different members of the STRONG subensemble. The wind plotting convention is as in Fig. 1.

Small MLCAPE in northeastern Alabama when possible entrainment effects are accounted for, by itself, does not preclude the occurrence of severe weather. The majority of convectively induced severe weather in the southeastern United States, including tornadoes, occurs during the winter and early spring in high vertical wind shear–low CAPE (HSLC) environments (e.g., Sherburn and Parker 2014; Sherburn et al. 2016). However, composite conditions in these HSLC environments contain large relative humidity and significant mesoscale upward motion through at least a several-kilometers-deep layer above the warm-sector PBL, which differs from the current case.

Upward motion in the current case is only ~2 km deep (Figs. 3, 18d), and appears related to alignments of the middle tropospheric trough and front being approximately parallel to the surface cold front (Fig. 1b). This configuration does not produce the constructive coupling of lower- and upper-tropospheric mesoscale circulations often observed in severe weather environments (e.g., Beebe and Bates 1955; Newton; 1967; Uccellini and Johnson 1979; Shapiro 1982, cf. their Figs. 22 and 23). The lack of a cold front aloft

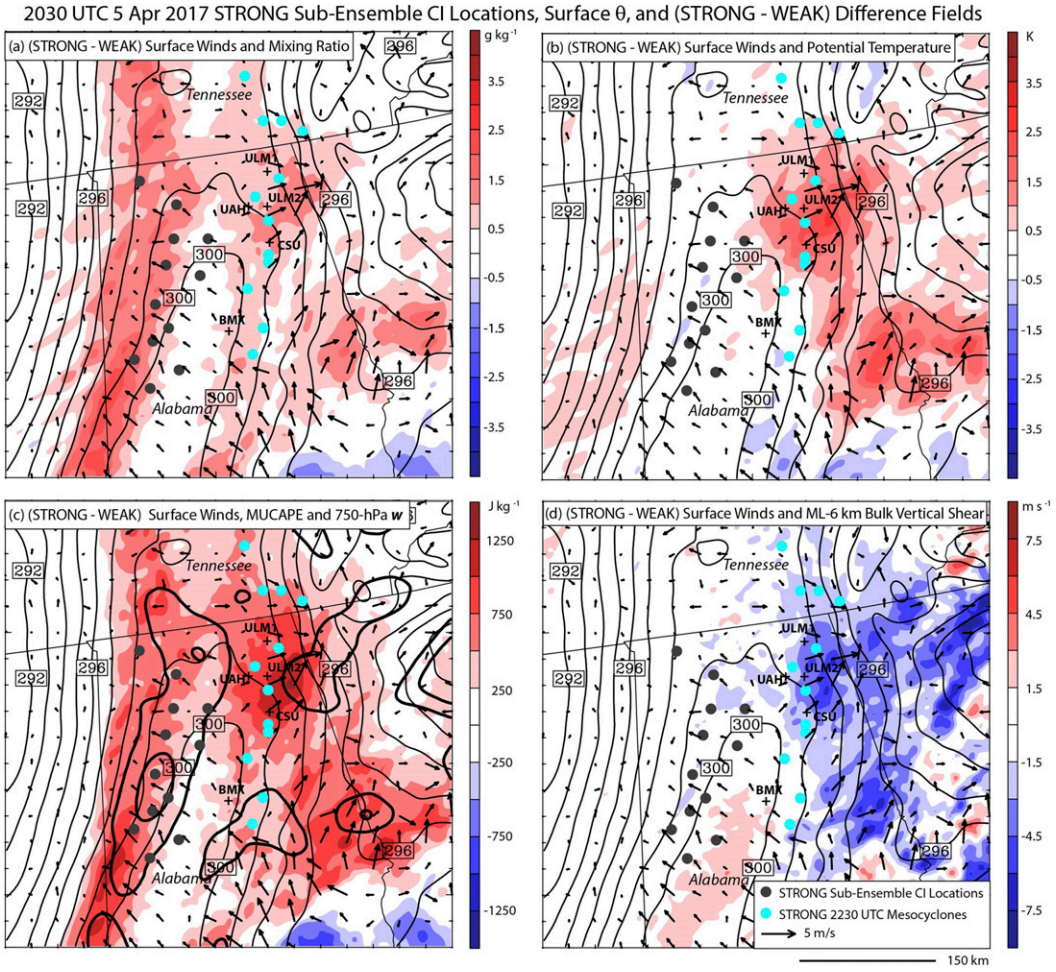

FIG. 21. Average STRONG subensemble surface potential temperature (1-K contour interval) with color-shaded (STRONG − WEAK) subensemble average difference fields of surface horizontal winds and (a) surface mixing ratio (g kg^{-1}), (b) potential temperature (K), (c) MUCAPE (J kg^{-1}, calculated as in Figs. 16a,c), and (d) mixed-layer (0–0.5 km) to 6-km layer bulk vertical shear magnitude (m s^{-1}) at 2030 UTC 5 Apr 2017. The dark gray bullets in each panel indicate the CI locations of the different members of the STRONG subensemble, and the cyan bullets indicate the positions of largest 2–5-km updraft helicity (UH_{max}) for each of the STRONG members at 2230 UTC 5 Apr 2017. The bold contours in (c) represent (STRONG − WEAK) subensemble average 750-hPa vertical motion (2.5 and 7.5 cm s^{-1} values).

(e.g., Locatelli et al. 2002; Schultz 2005) within the surface warm sector limits the thermodynamic instability in the current case, which contrasts with conditions in the devastating 26–27 April 2011 southeastern U.S. tornado outbreak (Chasteen and Koch 2021a).

Chasteen and Koch (2021b) describe how antecedent mesoscale organized convection modified the large-scale environment in a manner that supported the widespread afternoon outbreak of strong supercell tornadoes in the 26–27 April 2011 case. The antecedent MCS clearly impacts some locations in the convective environment of the current case. The boundary between the MCS wake and the more strongly heated air in advance of the surface front acts favorably to focus deep convection in some ensemble members (Fig. 10b, ellipse 1). However, the slow eastward progression of the antecedent MCS may be detrimental to overall severe weather potential by reducing the horizontal scale of thermodynamically unstable conditions ahead of the surface cold front (cf. Figs. 16a,c).

7. Summary

In this study we have used a convection permitting 50-member ensemble simulation, together with special field observations from IOP3b of VORTEX-SE_2017, to examine environmental factors leading to severe weather that occurred during the afternoon and early evening of 5 April 2017 over eastern Alabama. Comparison of convection initiation (CI) locations in the ensemble with those determined from NEXRAD WSR-88D reflectivity mosaics

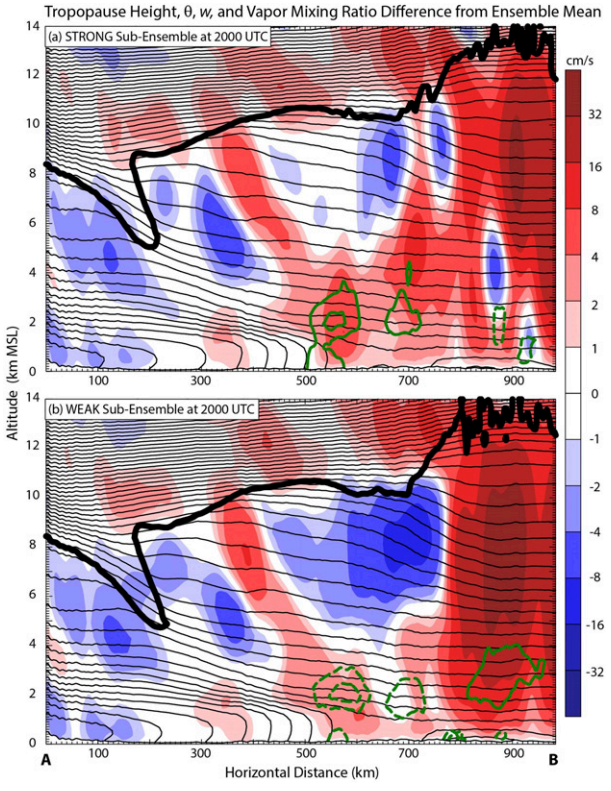

FIG. 22. Mean vertical cross sections along transect AB in Fig. 16, averaged for 100 km on each side of AB, at 2000 UTC 5 Apr 2017 (forecast hour t = 14 h) for (a) the 12-member subensemble STRONG and (b) the 8-member subensemble WEAK, whose maximum afternoon UH values are plotted individually in Figs. 9b and 9a, respectively. In both panels, vertical velocity is color shaded, potential temperature is indicated by the thin black contours (2-K contour interval), and the thick single black contour indicates the approximate tropopause height [2 potential vorticity units (PVU); 1 PVU = 10^{-6} K kg^{-1} m^2 s^{-1}]. The bold green contours indicate differences in water vapor mixing ratio (-1.5, -0.5, 0.5, and 1.5 g kg^{-1} values, negative dashed) from the same time in the corresponding vertical cross section of the ensemble mean (not shown).

revealed an accurate representation, within mesoscale bounds, of the actual CI.

The horizontal resolution of the model is similar to that employed in the highest-resolution deterministic operational models, such as the HRRR (Benjamin et al. 2016). Such models are unable to reliably simulate atmospheric scales of motion directly responsible for severe weather, so our approach used the model storm surrogate of 2–5-km-layer updraft helicity UH as a metric for storm severity. Using a previously established severe-weather threshold value of UH, we found that about half of the ensemble members were likely to produce severe weather, which is broadly consistent with the moderate intensity and limited (~6 h) duration of the observed severe weather on this day.

Combined with VSE field observations, the large ensemble-model spread in UH_{max} was exploited to conduct a physical process study that examined factors important to CI and subsequent storm severity. This was performed by analyzing the ensemble-mean environmental conditions, together with two smaller subensembles that contained members having UH_{max} values representative of severe-weather-producing midtropospheric mesocyclones in one subensemble (STRONG), and values representative of nonsevere storms in the other (WEAK).

The afternoon CI of interest occurred in advance of a strong eastward-translating synoptic cold front and midtropospheric trough. Both surface observations and the ensemble mean indicated this CI occurred near a prefrontal surface potential temperature maximum associated with strong daytime heating. VSE radiosonde data established that mesoscale ascent likely contributed to afternoon cooling above the PBL, which further enhanced thermodynamic destabilization ahead of the synoptic cold front. The mesoscale ascent along and in advance of the surface cold front was also captured in the ensemble mean, and was linked to frontogenesis occurring along the warm side of the surface front. Diagnosis of the ensemble mean also confirmed cooling associated with mesoscale ascent located directly above the strongly heated PBL in advance of the surface front, which helped focus the location of the CI.

Comparison of the STRONG and WEAK subensembles revealed that larger MLCAPE and stronger vertical motion in the CI region located directly ahead of a stronger frontal moisture gradient allowed timelier CI in STRONG. Development of midtropospheric mesocyclones was facilitated further by movement of incipient simulated storms toward a region that had both warmer and moister surface conditions in STRONG than in WEAK, which contributed to larger MLCAPE. Despite favorable conditions for severe weather, its areal coverage and duration over the VSE region was limited in this case by the rapid eastward translation of a synoptic cold front and the persistence of an antecedent MCS, due to the thermodynamic stabilization that occurred in the wake of these critically important weather features. MLCAPE, which was influenced in STRONG and WEAK by differences in the CI environment near the cold front and later by the antecedent MCS position, was able to successfully discriminate between these ensemble subsets.

If available in real time, the distribution of UH_{max} values in the ensemble could have provided potentially useful overall guidance for severe weather forecasts at lead times of 12–18 h. However, the model was unable to successfully discriminate, through UH_{max} values, the ~100-km-scale mesoscale regions where severe weather was reported from the larger surrounding areas in eastern Alabama. This is attributed to a positive bias in simulated MLCAPE over northeastern Alabama, where no severe weather was reported. In addition to differences in the observed and simulated MCS, this bias could also be influenced by flow interactions with the model terrain, which constitutes an important topic for future research.

Acknowledgments. The authors acknowledge participants of the VORTEX-SE 2017 field campaign, whose data collection

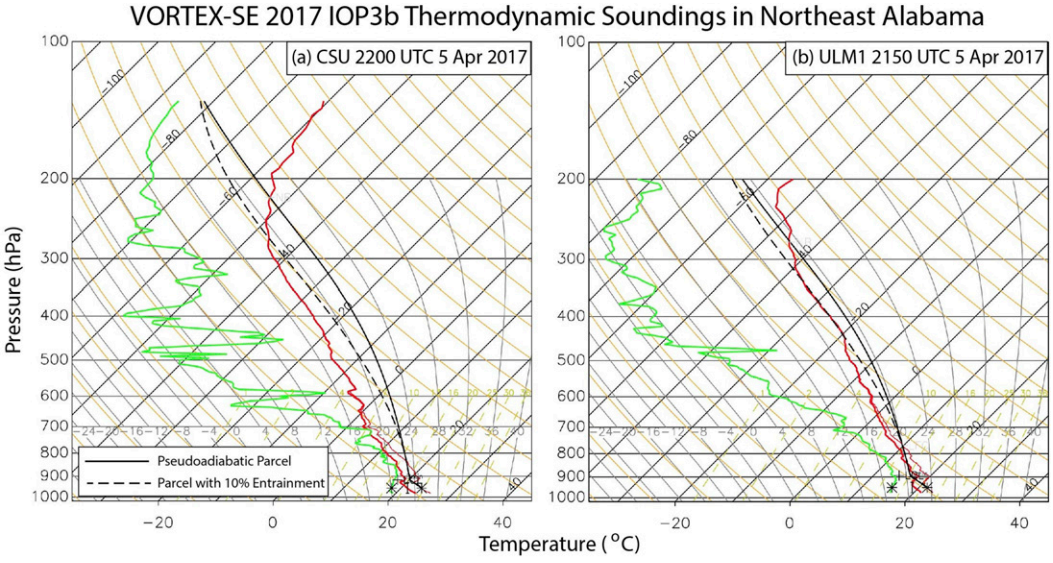

FIG. 23. Temperature (red) and dewpoint (green) for VSE soundings from the (a) CSU and (c) ULM1 locations shown in Fig. 5. The thin orange curve indicates the virtual temperature, and the bold and dashed black curves illustrate the pseudoadiabatic ascent of 50-hPa deep surface-based air parcels with (dashed) and without (solid) a constant rate of 10% entrainment of environmental air per kilometer during a hypothetical parcel ascent.

efforts help lead to the high-quality radiosonde data used in this study. The radar data displayed in Fig. 4 were converted with Py-ART (Helmus and Collis 2016), and surface observations used in overlays were obtained from the Iowa Environmental Mesonet made available by Iowa State University, Department of Agronomy. Manuscript reviews from Morris Weisman (NCAR) and three anonymous reviewers provided helpful clarifications in the paper. This work has been supported by NOAA Grant NA17OAR4590190 and by National Science Foundation funds for the U. S. Weather Research Program (USWRP), which supports NCAR's Short Term Explicit Prediction (STEP) program. The National Center for Atmospheric Research is sponsored by the National Science Foundation.

Data availability statement. The VORTEX-SE soundings used in this study can be obtained at https://www.eol.ucar.edu/field_projects/vortex-se2017. Netcdf output from the WRF Model ensemble simulation can be obtained from the first author (trier@ucar.edu) upon request.

REFERENCES

Agee, E., and L. Taylor, 2019: Historical analysis of U.S. tornado fatalities (1808–2017): Population, science, and technology. *Wea. Climate Soc.*, **11**, 355–368, https://doi.org/10.1175/WCAS-D-18-0078.1.

Anderson, J. L., T. Hoar, K. Raeder, H. Liu, N. Collins, R. Torn, and A. Arellano, 2009: The Data Assimilation Research Testbed: A community facility. *Bull. Amer. Meteor. Soc.*, **90**, 1283–1296, https://doi.org/10.1175/2009BAMS2618.1.

Anderson-Frey, A. K., Y. P. Richardson, A. R. Dean, R. L. Thompson, and B. T. Smith, 2019: Characteristics of tornado events and warning in the southeastern United States. *Wea. Forecasting*, **34**, 1017–1034, https://doi.org/10.1175/WAF-D-18-0211.1.

Ashley, W. S., 2007: Spatial and temporal analysis of tornado fatalities in the United States: 1880–2005. *Wea. Forecasting*, **22**, 1214–1228, https://doi.org/10.1175/2007WAF2007004.1.

——, A. M. Haberlie, and J. Strohm, 2019: A climatology of quasi-linear convective systems and their hazards in the United States. *Wea. Forecasting*, **34**, 1605–1631, https://doi.org/10.1175/WAF-D-19-0014.1.

Beebe, R. G., and F. C. Bates, 1955: A mechanism for assisting in the release of convective instability. *Mon. Wea. Rev.*, **83**, 1–10, https://doi.org/10.1175/1520-0493(1955)083<0001:AMFAIT>2.0.CO;2.

Benjamin, S. G., and Coauthors, 2016: A North American hourly assimilation and model forecast cycle: The Rapid Refresh. *Mon. Wea. Rev.*, **144**, 1669–1694, https://doi.org/10.1175/MWR-D-15-0242.1.

Brooks, H., C. A. Doswell III, and M. P. Kay, 2003: Climatological estimates of local daily tornado probability for the United States. *Wea. Forecasting*, **18**, 626–640, https://doi.org/10.1175/1520-0434(2003)018<0626:CEOLDT>2.0.CO;2.

Brown, M., 2018: MSU Mobile Radiosonde Data Version 1.1. UCAR/NCAR–Earth Observing Laboratory, acessed 21 November 2020, https://doi.org/10.5065/D6H70DKK.

Chasteen, M. B., and S. E. Koch, 2021a: Multiscale aspects of the 26–27 April 2011 tornado outbreak. Part I: Outbreak chronology and environmental evolution. *Mon. Wea. Rev.*, **149**, https://doi.org/10.1175/MWR-D-21-0013.1, in press.

——, and ——, 2021b: Multiscale aspects of the 26–27 April 2011 tornado outbreak. Part II: Environmental modifications and upscale feedbacks arising from latent processes. *Mon. Wea. Rev.*, **149**, https://doi.org/10.1175/MWR-D-21-0014.1, in press.

Childs, S. J., R. S. Schumacher, and J. T. Allen, 2018: Cold-season tornadoes: Climatological and meteorological insights. *Wea. Forecasting*, **33**, 671–691, https://doi.org/10.1175/WAF-D-17-0120.1.

Cohen, A. E., S. M. Cavallo, M. C. Coniglio, and H. E. Brooks, 2015: A review of planetary boundary layer parameterization

schemes and their sensitivity in simulating southeastern U.S. cold season severe weather environments. *Wea. Forecasting*, **30**, 591–612, https://doi.org/10.1175/WAF-D-14-00105.1.

——, ——, ——, ——, and I. L. Jirak, 2017: Evaluation of multiple planetary boundary layer parameterization schemes in southeast U.S. cold season severe thunderstorm environments. *Wea. Forecasting*, **32**, 1857–1884, https://doi.org/10.1175/WAF-D-16-0193.1.

Coleman, A., and B. Ancell, 2020: Toward the improvement of high-impact probabilistic forecasts with a sensitivity-based convective-scale ensemble subsetting technique. *Mon. Wea. Rev.*, **148**, 4995–5014, https://doi.org/10.1175/MWR-D-20-0043.1.

Coleman, T. A., A. W. Lyza, K. R. Knupp, K. Laws, and W. Wyatt, 2018: A significant tornado in a heterogeneous environment during VORTEX-SE. *Electron. J. Severe Storms Meteor.*, **13** (2), https://www.ejssm.org/ojs/index.php/ejssm/article/view/165.

Coniglio, M. C., J. Correia, P. T. Marsh, and F. Kong, 2013: Verification of convection-allowing WRF Model forecasts of the planetary boundary layer using sounding observations. *Wea. Forecasting*, **28**, 842–862, https://doi.org/10.1175/WAF-D-12-00103.1.

Davis, C. A., and D. A. Ahijevych, 2013: Thermodynamic environments of deep convection in Atlantic tropical disturbances. *J. Atmos. Sci.*, **70**, 1912–1928, https://doi.org/10.1175/JAS-D-12-0278.1.

Davis, J. M., and M. D. Parker, 2014: Radar climatology of tornadic and nontornadic vortices in high-shear, low-CAPE environments in the mid-Atlantic and southeastern United States. *Wea. Forecasting*, **29**, 828–853, https://doi.org/10.1175/WAF-D-13-00127.1.

Ek, M. B., K. E. Mitchell, Y. Lin, E. Rogers, P. Grummann, V. Koren, G. Gayno, and J. D. Tarpley, 2003: Implementation of Noah land-surface model advances in the NCEP operational mesoscale Eta model. *J. Geophys. Res.*, **108**, 8851, https://doi.org/10.1029/2002JD003296.

Ellis, K., D. Burow, K. Gassert, L. Mason, and M. Porter, 2019: Forecaster perceptions and climatological analysis of the influence of convective mode on tornado climatology and warning success. *Ann. Amer. Assoc. Geogr.*, **110**, 1075–1094, https://doi.org/10.1080/24694452.2019.1670042.

Gaffin, D. M., and S. S. Parker, 2006: A climatology of synoptic conditions associated with significant tornadoes across the southern Appalachian region. *Wea. Forecasting*, **21**, 735–751, https://doi.org/10.1175/WAF951.1.

Galway, J. G., and A. Pearson, 1981: Winter tornado outbreaks. *Mon. Wea. Rev.*, **109**, 1072–1080, https://doi.org/10.1175/1520-0493(1981)109<1072:WTO>2.0.CO;2.

Geerts, B., and Coauthors, 2017: The 2015 Plains Elevated Convection At Night Field Project. *Bull. Amer. Meteor. Soc.*, **98**, 767–786, https://doi.org/10.1175/BAMS-D-15-00257.1.

Grams, J. S., R. L. Thompson, D. V. Snively, J. A. Prentice, G. M. Hodges, and L. J. Reames, 2012: A climatology and comparison of parameters for significant tornado events in the United States. *Wea. Forecasting*, **27**, 106–123, https://doi.org/10.1175/WAF-D-11-00008.1.

Guyer, J. L., and A. R. Dean, 2010: Tornadoes within weak CAPE environments across the continental United States. *25th Conf. on Severe Local Storms*, Denver, CO, Amer. Meteor. Soc., 1.5, https://ams.confex.com/ams/25SLS/techprogram/paper_175725.htm.

Hakim, G. J., and R. D. Torn, 2008: Ensemble synoptic analysis. *Synoptic-Dynamic Meteorology and Weather Analysis and Forecasting: A Tribute to Fred Sanders, Meteor. Monogr.*, No. 55, Amer. Meteor. Soc., 147–161.

Helmus, J. J., and S. M. Collis, 2016: The Python ARM Radar Toolkit (Py-ART), a library for working with weather radar data in the Python programming language. *J. Open Res. Software*, **4**, e25, https://doi.org/10.5334/jors.119.

Holton, J. R., 1992: *An Introduction to Dynamic Meteorology*. 3rd ed. Academic Press, 511 pp.

Iacono, M. J., J. S. Delamere, E. J. Mlawer, M. W. Shepard, S. A. Clough, and W. D. Collins, 2008: Radiative forcing by long-wave greenhouse gases: Calculations with the AER radiative transfer models. *J. Geophys. Res.*, **113**, D13103, https://doi.org/10.1029/2008JD009944.

Janjić, Z. I., 2001: Nonsingular implementation of the Mellor–Yamada level 2.5 scheme in the NCEP Meso Model. NCEP Office Note 437, 61 pp., http://www.emc.ncep.noaa.gov/officenotes/newernotes/on437.pdf.

Kain, J. S., and Coauthors, 2008: Some practical considerations regarding horizontal resolution in the first generation of operational convection-allowing NWP. *Wea. Forecasting*, **23**, 931–952, https://doi.org/10.1175/WAF2007106.1.

Keyser, D., M. J. Reeder, and R. J. Reed, 1988: A generalization of Petterssen's frontogenesis function and its relation to the forcing of vertical motion. *Mon. Wea. Rev.*, **116**, 762–781, https://doi.org/10.1175/1520-0493(1988)116<0762:AGOPFF>2.0.CO;2.

King, J. R., M. D. Parker, K. D. Sherburn, and G. M. Lackmann, 2017: Rapid evolution of cool season, low-CAPE severe thunderstorm environments. *Wea. Forecasting*, **32**, 763–779, https://doi.org/10.1175/WAF-D-16-0141.1.

Kis, A. K., and J. M. Straka, 2010: Nocturnal tornado climatology. *Wea. Forecasting*, **25**, 545–561, https://doi.org/10.1175/2009WAF2222294.1.

Knupp, K. R., and Coauthors, 2014: Meteorological overview of the devastating 27 April 2011 tornado outbreak. *Bull. Amer. Meteor. Soc.*, **95**, 1041–1062, https://doi.org/10.1175/BAMS-D-11-00229.1.

Krocak, M. J., and H. E. Brooks, 2018: Climatological estimates of hourly tornado probability for the United States. *Wea. Forecasting*, **33**, 59–69, https://doi.org/10.1175/WAF-D-17-0123.1.

Lawson, J. R., C. K. Potvin, P. S. Skinner, and A. E. Reihardt, 2021: The vice and virtue of increased horizontal resolution in ensemble forecasts of tornadic thunderstorms in low-CAPE, high-shear environments. *Mon. Wea. Rev.*, **149**, 921–944, https://doi.org/10.1175/MWR-D-20-0281.1.

Lemon, L. R., and C. A. Doswell III, 1979: Severe thunderstorm evolution and mesocyclone structure as related to tornadogenesis. *Mon. Wea. Rev.*, **107**, 1184–1197, https://doi.org/10.1175/1520-0493(1979)107<1184:STEAMS>2.0.CO;2.

Locatelli, J. D., R. D. Schwartz, M. T. Stoelinga, and P. V. Hobbs, 2002: Norwegian-type and cold front aloft-type cyclones east of the Rocky Mountains. *Wea. Forecasting*, **17**, 66–82, https://doi.org/10.1175/1520-0434(2002)017<0066:NTACFA>2.0.CO;2.

McDonald, J. M., and C. C. Weiss, 2021: Cold-pool characteristics of tornadic quasi-linear convective systems and other convective modes during VORTEX-SE. *Mon. Wea. Rev.*, **149**, 821–840, https://doi.org/10.1175/MWR-D-20-0226.1.

Mlawer, E. J., S. J. Taubman, P. D. Brown, M. J. Iacono, and S. A. Clough, 1997: Radiative transfer for inhomogeneous atmosphere: RRTM, a validated correlated-k model for the longwave.

J. Geophys. Res., **102**, 16663–16682, https://doi.org/10.1029/97JD00237.

Mulholland, J. P., J. M. Peters, and H. Morrison, 2021: How does vertical wind shear influence entrainment in squall lines? *J. Atmos. Sci.*, **78**, 1931–1946, https://doi.org/10.1175/JAS-D-20-0299.1.

Murphy, T., 2018: ULM Mobile Radiosonde Data, version 1.2. UCAR/NCAR–Earth Observing Laboratory, accessed 21 November 2020, https://doi.org/10.5065/D6ZK5FD4.

Newton, C. W., Ed., 1967: Severe convective storms. *Advances in Geophysics*, Vol. 12, Academic Press, 257–303.

Ogura, Y., and D. Portis, 1982: Structure of a cold front observed in SESAME-AVE III and its comparison with the Hoskins–Bretherton frontogenesis model. *J. Atmos. Sci.*, **39**, 2773–2792, https://doi.org/10.1175/1520-0469(1982)039<2773:SOTCFO>2.0.CO;2.

Pangle, P., and R. Wade, 2020: UAH Mobile Radiosonde Data, version 1.1. UCAR/NCAR–Earth Observing Laboratory, accessed 21 November 2020, https://doi.org/10.26023/A3EA-SK0M-BR14.

Powers, J., and Coauthors, 2017: The Weather Research and Forecasting (WRF) Model: Overview, system efforts, and future directions. *Bull. Amer. Meteor. Soc.*, **98**, 1717–1737, https://doi.org/10.1175/BAMS-D-15-00308.1.

Rasmussen, E. N., and D. O. Blanchard, 1998: A baseline climatology of sounding-derived supercell and tornado forecast parameters. *Wea. Forecasting*, **13**, 1148–1164, https://doi.org/10.1175/1520-0434(1998)013<1148:ABCOSD>2.0.CO;2.

Romine, G. S., C. S. Schwartz, J. Berner, K. R. Fossell, C. Snyder, J. L. Anderson, and M. L. Weisman, 2014: Representing forecast error in a convection-permitting ensemble system. *Mon. Wea. Rev.*, **142**, 4519–4541, https://doi.org/10.1175/MWR-D-14-00100.1.

Romps, D. M., 2010: A direct measurement of entrainment. *J. Atmos. Sci.*, **67**, 1908–1927, https://doi.org/10.1175/2010JAS3371.1.

Rotunno, R., and J. B. Klemp, 1982: The influence of the shear-induced pressure gradient on thunderstorm motion. *Mon. Wea. Rev.*, **110**, 136–151, https://doi.org/10.1175/1520-0493(1982)110<0136:TIOTSI>2.0.CO;2.

——, and ——, 1985: On the rotation and propagation of simulated supercell thunderstorms. *J. Atmos. Sci.*, **42**, 271–292, https://doi.org/10.1175/1520-0469(1985)042<0271:OTRAPO>2.0.CO;2.

Schultz, D. M., 2005: A review of cold fronts with prefrontal troughs and wind shifts. *Mon. Wea. Rev.*, **133**, 2449–2472, https://doi.org/10.1175/MWR2987.1.

Schumacher, R., and E. Nielsen, 2018: CSU Mobile Radiosonde Data version 2.0. UCAR/NCAR–Earth Observing Laboratory, accessed 21 November 2020, https://doi.org/10.5065/D62J69KP.

Schwartz, C. S., G. S. Romine, M. L. Weisman, R. A. Sobash, K. R. Fossell, K. W. Manning, and S. B. Trier, 2015a: A real-time convection-allowing ensemble prediction system initialized by mesoscale Kalman filter analyses. *Wea. Forecasting*, **30**, 1158–1181, https://doi.org/10.1175/WAF-D-15-0013.1.

——, ——, R. A. Sobash, K. R. Fossell, and M. L. Weisman, 2015b: NCAR's experimental real-time convection-allowing ensemble prediction system. *Wea. Forecasting*, **30**, 1645–1654, https://doi.org/10.1175/WAF-D-15-0103.1.

——, ——, ——, ——, and ——, 2019: NCAR's real-time convection-allowing ensemble project. *Bull. Amer. Meteor. Soc.*, **100**, 321–343, https://doi.org/10.1175/BAMS-D-17-0297.1.

Shapiro, M. A., 1982: Mesoscale weather systems of the central United States. CIRES/NOAA Tech. Rep., University of Colorado, 78 pp.

Sherburn, K. D., and M. D. Parker, 2014: Climatology and ingredients of significant severe convection in high-shear low-CAPE environments. *Wea. Forecasting*, **29**, 854–877, https://doi.org/10.1175/WAF-D-13-00041.1.

——, ——, J. R. King, and G. M. Lackmann, 2016: Composite environments of severe and nonsevere high-shear, low-CAPE convective events. *Wea. Forecasting*, **31**, 1899–1927, https://doi.org/10.1175/WAF-D-16-0086.1.

Skamarock, W. C., and J. B. Klemp, 2008: A time-split nonhydrostatic atmospheric model for weather research and forecasting applications. *J. Comput. Phys.*, **227**, 3465–3485, https://doi.org/10.1016/j.jcp.2007.01.037.

Smith, B. T., R. L. Thompson, J. S. Grams, C. Broyles, and H. E. Brooks, 2012: Convective modes for significant severe thunderstorms in the contiguous United States. Part I: Storm classification and climatology. *Wea. Forecasting*, **27**, 1114–1135, https://doi.org/10.1175/WAF-D-11-00115.1.

Sobash, R. A., J. S. Kain, D. R. Bright, A. R. Dean, M. C. Coniglio, and S. J. Weiss, 2011: Probabilistic forecast guidance for severe thunderstorms based on the identification of extreme phenomena in convection-allowing model forecasts. *Wea. Forecasting*, **26**, 714–728, https://doi.org/10.1175/WAF-D-10-05046.1.

——, C. S. Schwartz, G. S. Romine, K. R. Fossell, and M. L. Weisman, 2016: Severe weather prediction using storm surrogates from an ensemble forecasting system. *Wea. Forecasting*, **31**, 255–271, https://doi.org/10.1175/WAF-D-15-0138.1.

——, ——, ——, and M. L. Weisman, 2019: Next-day prediction of tornadoes using convection-allowing models with 1-km horizontal grid spacing. *Wea. Forecasting*, **34**, 1117–1135, https://doi.org/10.1175/WAF-D-19-0044.1.

Stensrud, D. J., and R. A. Maddox, 1988: Opposing mesoscale circulations: A case study. *Wea. Forecasting*, **3**, 189–204, https://doi.org/10.1175/1520-0434(1988)003<0189:OMCACS>2.0.CO;2.

Strader, S., and W. Ashley, 2018: Finescale assessment of mobile home tornado vulnerability in the central and southeast United States. *Wea. Climate Soc.*, **10**, 797–812, https://doi.org/10.1175/WCAS-D-18-0060.1.

Thompson, G., P. R. Field, R. M. Rasmussen, and W. D. Hall, 2008: Explicit forecasts of winter precipitation using an improved bulk microphysics scheme. Part II: Implementation of a snow parameterization. *Mon. Wea. Rev.*, **136**, 5095–5115, https://doi.org/10.1175/2008MWR2387.1.

Thompson, R. L., R. Edwards, J. A. Hart, K. L. Elmore, and P. Markowski, 2003: Close proximity soundings within supercell environments obtained from the Rapid Update Cycle. *Wea. Forecasting*, **18**, 1243–1261, https://doi.org/10.1175/1520-0434(2003)018<1243:CPSWSE>2.0.CO;2.

——, C. M. Mead, and R. Edwards, 2007: Effective storm-relative helicity and bulk shear in supercell thunderstorm environments. *Wea. Forecasting*, **22**, 102–115, https://doi.org/10.1175/WAF969.1.

——, B. T. Smith, J. S. Grams, A. R. Dean, and C. Broyles, 2012: Convective modes for significant severe thunderstorms in the contiguous United States. Part II: Supercell and QLCS tornado environments. *Wea. Forecasting*, **27**, 1136–1154, https://doi.org/10.1175/WAF-D-11-00116.1.

Tiedtke, M., 1989: A comprehensive mass flux scheme for cumulus parameterization in large-scale models. *Mon. Wea. Rev.*, **117**, 1779–1800, https://doi.org/10.1175/1520-0493(1989)117<1779:ACMFSF>2.0.CO;2.

Torn, R. D., G. J. Hakim, and C. Snyder, 2006: Boundary conditions for limited-area ensemble Kalman filters. *Mon. Wea. Rev.*, **134**, 2490–2502, https://doi.org/10.1175/MWR3187.1.

Trapp, R. J., S. A. Tessendorf, E. S. Godfrey, and H. E. Brooks, 2005: Tornadoes from squall lines and bow echoes. Part I: Climatological distribution. *Wea. Forecasting*, **20**, 23–34, https://doi.org/10.1175/WAF-835.1.

Trier, S. B., D. B. Parsons, and J. H. E. Clark, 1991: Environment and evolution of a cold-frontal mesoscale convective system. *Mon. Wea. Rev.*, **119**, 2429–2455, https://doi.org/10.1175/1520-0493(1991)119<2429:EAEOAC>2.0.CO;2.

——, G. S. Romine, D. A. Ahijevych, R. J. Trapp, R. S. Schumacher, M. C. Coniglio, and D. J. Stensrud, 2015: Mesoscale thermodynamic influences on convection initiation near a surface dryline in convection-permitting ensemble. *Mon. Wea. Rev.*, **143**, 3726–3753, https://doi.org/10.1175/MWR-D-15-0133.1.

——, J. W. Wilson, D. A. Ahijevych, and R. A. Sobash, 2017: Mesoscale vertical motions near nocturnal convection initiation in PECAN. *Mon. Wea. Rev.*, **145**, 2919–2941, https://doi.org/10.1175/MWR-D-17-0005.1.

——, G. S. Romine, D. A. Ahijevych, and R. A. Sobash, 2019: Lower-tropospheric influences on the timing and intensity of afternoon severe convection over modest terrain in a convection-allowing ensemble. *Wea. Forecasting*, **34**, 1633–1656, https://doi.org/10.1175/WAF-D-19-0087.1.

——, S. D. Kehler, and J. Hanesiak, 2020: Observations and simulation of elevated nocturnal convection initiation on 24 June 2015 during PECAN. *Mon. Wea. Rev.*, **148**, 613–635, https://doi.org/10.1175/MWR-D-19-0218.1.

UCAR/NCAR–Earth Observing Laboratory, 2017: National Weather Service High Resolution Radiosonde Data (ESC format), version 1.0. UCAR/NCAR–Earth Observing Laboratory, accessed 21 November 2020, https://doi.org/10.5065/D6DR2SXM.

Uccellini, L. W., and D. R. Johnson, 1979: The coupling of upper and lower tropospheric jet streaks and implications for the development of severe convective storms. *Mon. Wea. Rev.*, **107**, 682–703, https://doi.org/10.1175/1520-0493(1979)107<0682:TCOUAL>2.0.CO;2.

Yeo, K., and D. M. Romps, 2013: Measurement of convective entrainment using Lagrangian particles. *J. Atmos. Sci.*, **70**, 266–277, https://doi.org/10.1175/JAS-D-12-0144.1.

Zhang, C., Y. Wang, and K. Hamilton, 2011: Improved representation of boundary layer clouds over the southeast Pacific in ARW-WRF using a modified Tiedtke cumulus parameterization scheme. *Mon. Wea. Rev.*, **139**, 3489–3513, https://doi.org/10.1175/MWR-D-10-05091.1.